Title
Anxiety Cells in a Hippocampal-Hypothalamic Circuit

Permalink
https://escholarship.org/uc/item/33q053tz

Authors
Jimenez, Jessica
Su, Katy
Goldberg, Alexander
et al.

Publication Date
2017

Peer reviewed

Anxiety cells in a hippocampal-hypothalamic circuit

Jessica C. Jimenez[1,2], **Katy Su**[1,2,13], **Alexander R. Goldberg**[1,2,13], **Victor M. Luna**[1,2], **Jeremy S. Biane**[3], **Gokhan Ordek**[1,2], **Pengcheng Zhou**[4,5], **Samantha K. Ong**[1,2], **Matthew A. Wright**[6], **Larry Zweifel**[7,8], **Liam Paninski**[5], **Rene Hen**[1,2,14,*], and **Mazen A. Kheirbek**[3,9,10,11,12,*]

[1]Departments of Neuroscience, Psychiatry & Pharmacology, Columbia University, New York, NY, USA

[2]Division of Integrative Neuroscience, Department of Psychiatry, New York State Psychiatric Institute, New York, NY, USA

[3]Department of Psychiatry, University of California, San Francisco

[4]Center for the Neural Basis of Cognition and Machine Learning Department, Carnegie Mellon University, Pittsburgh, PA, USA

[5]Departments of Statistics and Neuroscience, Grossman Center for the Statistics of Mind, Center for Theoretical Neuroscience, Kavli Institute for Brain Science, and NeuroTechnology Center, Columbia University, New York, NY, USA

[6]Department of Psychiatry and Behavioral Sciences, Stanford University

[7]Department of Pharmacology, University of Washington, Seattle, WA 98105, USA

[8]Department of Psychiatry and Behavioral Sciences, University of Washington, Seattle, WA 98105, USA

[9]Neuroscience Graduate Program, San Francisco

[10]Weill Institute for Neurosciences, San Francisco

[11]Kavli Institute for Fundamental Neuroscience, San Francisco

[12]Center for Integrative Neuroscience University of California, San Francisco

Abstract

[*]Correspondence: R.H. (rh95@columbia.edu) and M.A.K. (Mazen.Kheirbek@ucsf.edu).
[13]These authors contributed equally to this work
[14]Lead contact

The hippocampus is traditionally thought to transmit contextual information to limbic structures where it acquires valence. Using freely moving calcium imaging and optogenetics, we show that while the dorsal CA1 subregion of the hippocampus is enriched in place cells, ventral CA1 (vCA1) is enriched in anxiety cells that are activated by anxiogenic environments and required for avoidance behavior. Imaging cells defined by their projection target revealed that anxiety cells were enriched in the vCA1 population projecting to the lateral hypothalamic area (LHA), but not to the basal amygdala (BA). Consistent with this selectivity, optogenetic activation of vCA1 terminals in LHA, but not BA increased anxiety and avoidance, while activation of terminals in BA, but not LHA impaired contextual fear memory. Thus, the hippocampus encodes not only neutral but also valence-related contextual information, and the vCA1-LHA pathway is a direct route by which the hippocampus can rapidly influence innate anxiety behavior.

eTOC blurb

Jimenez et al. show that vCA1 neurons exhibit stable representations of anxiogenic environments that are required for avoidance behavior. The direct projection from vCA1 to the lateral hypothalamus is enriched in anxiety cells and can rapidly control anxiety-related behavior.

Introduction

Fear and anxiety are emotional responses to perceived threats, with proximal threats eliciting fear and distal threats eliciting anxiety. Under normal conditions, anxiety states promote adaptive avoidance behaviors that are critical to safely navigating an environment. Execution of appropriate avoidance behaviors requires the rapid recognition of threatening stimuli, and routing that information to structures that can directly modulate these defensive behaviors. While avoidance is adaptive under normal conditions, it can become maladaptive when responses are excessive and inappropriate. In humans, a shared feature of a number of anxiety disorders is the overestimation of threat, leading to enhanced avoidance (Jovanovic and Ressler, 2010; Kheirbek et al., 2012). Yet the mechanisms and neural circuits by which normal adaptive avoidance behaviors arise, and how these circuits become disordered in psychiatric illness remain elusive.

While the hippocampus (HPC) is known to be critical for cognitive processes such as episodic memory and spatial navigation, it is also implicated in the pathogenesis of mood and anxiety disorders. One way the HPC may contribute to both cognitive and mood-related processes is via functional heterogeneity along its dorsoventral axis, with the dorsal HPC contributing to cognitive functions such as learning and memory, and the ventral HPC (vHPC) modulating emotional regulation (Fanselow and Dong, 2010; Strange et al., 2014). Lesions of the ventral, but not dorsal HPC are anxiolytic, with minimal effect on spatial learning (Bannerman et al., 2002; Kjelstrup et al., 2002; Moser et al., 1995), while dorsal HPC lesions affect spatial learning without affecting anxiety-related measures. Moreover, place cells, which are believed to contribute to a spatial representation of the environment, are more abundant, stable, and tuned in dorsal HPC relative to vHPC (Ciocchi et al., 2015; Jung et al., 1994; Keinath et al., 2014; Royer et al., 2010). In addition, recent optogenetic and pharmacological studies indicate that manipulation of the vHPC itself, or its inputs and cortical outputs can directly impact anxiety-related behavior (Felix-Ortiz et al., 2013;

Kheirbek et al., 2013; Kjaerby et al., 2016; Padilla-Coreano et al., 2016; Parfitt et al., 2017; Samuels et al., 2015; Wu and Hen, 2014).

Despite accumulating evidence supporting a role for vHPC in mood and anxiety-like behaviors, little is known about how the vHPC represents emotionally salient information and how those representations contribute to behavior. In the rodent model, anxiety-related behavior can be assessed with conflict-based avoidance tasks, which promote normal adaptive avoidance behavior to distal threats (Calhoon and Tye, 2015). Therefore, elucidating how innately anxiogenic contexts are represented within the vHPC will be critical to understanding how it may guide avoidance behaviors during conflict-based anxiety tasks.

Ventral CA1 (vCA1) sends dense projections to a number of subcortical structures such as the basal amygdala (BA), hypothalamus, nucleus accumbens (NAc), and bed nucleus of the stria terminalis (BNST) (Canteras, 2002; Cenquizca and Swanson, 2006, 2007; Kishi et al., 2006; Tannenholz et al., 2014). However, little is known about how vCA1 interacts with these regions to orchestrate emotional behaviors. In particular, despite decades of work demonstrating hippocampal-hypothalamic interactions in the buffering of stress responses via indirect inhibition of the hypothalamic-pituitary-adrenal axis (Jacobson and Sapolsky, 1991; Ulrich-Lai and Herman, 2009), the function of the direct HPC-hypothalamic pathway in modulating behavior remains unknown. vCA1 sends dense projections to the BA and lateral hypothalamic area (LHA) directly, and recent optogenetic studies have indicated that both the BA and LHA can control anxiety-related behavior in real-time (Jennings et al., 2013; Tye et al., 2011). However, how anxiety-related information is represented within vCA1 projection neurons to impact these output structures remains unclear.

Here, we applied freely moving calcium imaging and optogenetics to investigate how anxiety-related information is represented within distinct populations of vCA1 projection neurons. Intriguingly, we found "anxiety cells" enriched within a population of vCA1-LHA projecting neurons that represent anxiogenic environments and causally impact avoidance behavior. This reveals that the vCA1-LHA projection stream may serve as a direct route for vCA1 to rapidly control anxiety-like behaviors.

Results

Representations of anxiety-related information in vCA1

We first determined how vCA1 is engaged during exploration of innately anxiogenic environments. We used microendoscopy to perform calcium imaging of GCaMP6f expressing vCA1 neurons in freely moving mice. A gradient refractive index (GRIN) lens was implanted over the vCA1 subregion (Fig. 1A, S1A), and the Ca^{2+} indicator GCaMP6f was virally expressed to visualize vCA1 Ca^{2+} activity as previously described (Resendez et al., 2016; Ziv et al., 2013). This approach allowed us to record Ca^{2+} transient events in individual vCA1 neurons in the same field of view (FOV) while mice freely explored multiple environments (Fig. 1A, see methods).

In the Elevated Plus Maze (EPM), we found that a majority of vCA1 neurons exhibited a significant increase in Ca^{2+} activity and rate of Ca^{2+} transients during exploration of the anxiogenic open arm compartment as compared to the closed arm compartment (Fig. 1B, 1C, S1B, S1D). We next compared the average calcium activity across successive behavioral entrances and exploration bouts of the open arms. We found that vCA1 activity increases during exploration of both open arms, and decreases upon re-entry into the closed arm compartment (Fig. 1D). This activity increase was not merely driven by a change in spatial location, as switching between closed arm compartments did not elicit heightened activity, while open arm switching sustained heightened activity (Fig. 1D). This was not due to differences in mouse velocity between compartments, as open and closed arm velocity distributions were similar across animals (Fig. S1C). We next considered whether vCA1 heightened open arm activity was related to an increase in spatial salience in the open arm (relative to the closed arm), rather than its aversive nature. We imaged vCA1 while mice explored a familiar open field arena which included a spatially salient novel object that elicited approach (Fig. 1E). Unlike our findings in the open arms of the EPM, exploration of the quadrant containing the appetitive novel object did not evoke increases in vCA1 activity (Fig. 1F), indicating that vCA1 neurons are biased to represent anxiogenic features of the environment rather than changes in spatial salience.

We next investigated if the magnitude of open arm evoked activity was correlated with the anxiety level of individual animals. vCA1 open arm evoked activity (open-closed Ca^{2+} transient rate) was tightly correlated with the degree to which mice avoided the open arms of the maze (a measure of baseline anxiety levels) (Fig. 1G), with more anxious animals exhibiting higher levels of activity. Importantly, these effects on open and closed arm Ca^{2+} rate differences were not an artifact of sparse behavioral sampling, as calculating closed arm Ca^{2+} event rates from a matching number of behavioral samples resulted in the same correlation between open arm evoked activity and avoidance of the open arms (Fig. S1F). Moreover, while the mean open arm Ca^{2+} event rate was positively correlated with avoidance behavior, closed arm rates were not correlated with open arm avoidance (Fig. S1G, S1H). Finally, vCA1 open arm activity was found to further increase when mice engaged in highly anxiogenic head dipping behaviors at the edges of the open arms (Fig 1D, 1H, S1E). These results suggest that vCA1 generates representations of anxiogenic stimuli via a rate code that is both correlated with baseline anxiety state and scales with the aversive nature of the behavior.

Real-time control of avoidance behavior by vCA1

We next tested whether vCA1 open arm evoked activity was necessary for the maintenance of open arm avoidance in the EPM. Mice were bilaterally injected in vCA1 with either a control virus or one expressing ArchT, and implanted with fiber optics in the same location (Fig. 2A, S2C). This allowed us to silence vCA1-ArchT expressing pyramidal neurons with 532nm light illumination (Fig. S2A, S2B). We selectively triggered optogenetic silencing of vCA1 activity only when mice entered the open arms of the EPM (Fig. 2B). When compared to eYFP controls, vCA1-ArchT silenced mice spent significantly more time exploring the open arms of the EPM (Fig. 2B). This effect was also found in the Open Field Test (OFT), as selectively silencing vCA1 neurons during exploration of the anxiogenic center zone

significantly increased the amount of time mice spent exploring the center (Fig. S2E, S2F). This was not due to appetitive effects of light-induced inhibition of vCA1, as Arch and eYFP mice spent a similar amount of time on the side with light illumination in a real-time place preference assay (RTPP) (Fig. 2C). In addition, these effects were not due to changes in locomotor activity or increases in the number of open arm visitations (Fig. S2D, S2F). To assess whether these changes in anxiety-related behavior were specific to silencing open arm evoked activity, or due to an inability of mice to recognize where they were in the maze, we then tested a second group of mice with laser stimulation only during closed arm exploration bouts (Fig. 2B). In contrast to open arm silencing in the EPM, closed arm silencing caused no changes in anxiety behavior (Fig. 2B). These data suggest that vCA1 heightened activity in anxiogenic environments promotes avoidance behavior.

Differential representations of anxiety-related information across the dorsoventral axis of CA1

We next assessed the specialization and stability of anxiety-related activity along the dorsoventral axis of the hippocampus. We imaged dCA1 neurons in the EPM in an identical fashion as described above, and compared activity to vCA1 imaged neurons (Fig. 3A, S4A). At the population level, we found that dCA1 neurons did not exhibit significant changes in Ca^{2+} transient event rate in the open arms of the EPM (Fig. 3B), and did not correlate with the anxiety level of individual animals (linear regression as in Fig. 1H, R^2=0.066). Using statistical methods to classify neurons as significantly more active in selective compartments (see Methods) we found that ~51% of recorded vCA1 neurons were open arm selective (Fig. 3C & S4B), and this proportion was significantly greater relative to the dCA1 population which exhibited a more evenly distributed selectivity preference (Fig. 3C & S4B).

We next considered whether CA1 open arm selective neurons in the EPM were specialized to respond to anxiogenic stimuli in multiple contexts. Individual vCA1 and dCA1 neurons were tracked across multiple imaging sessions, and the activity of EPM open arm selective neurons was assessed in the anxiety provoking OFT, and the appetitive novel object task (Fig. 3D, S3A–E). Interestingly, we found that vCA1 open arm selective neurons exhibited a significantly higher rate of Ca^{2+} transient events during exploration of the anxiogenic center zone of the OFT compared to the periphery, but not during exploration of a preferred novel object (Fig. 3E). Moreover, these effects were specific to vCA1 open arm preferring neurons, as dCA1 open arm neurons did not exhibit changes in Ca^{2+} activity in the OFT center (Fig. 3E). In an alternative unbiased approach, we defined vCA1 and dCA1 task-selective neurons in the EPM, OFT, and novel object task based on their activity preference for the anxiogenic (open arms; center) or appetitive (novel object zone) compartments, and compared the overlap of selective cells recruited across tasks (Fig. S3F). We found that the population of vCA1 neurons that were selective for the EPM open arms were significantly overlapping with neurons that were selective for the OFT center, but not with neurons selective to a novel object, indicating that vCA1 open arm selective neurons are preferentially recruited in anxiogenic environments (Fig. S3G). In contrast, dCA1 neurons that were selective for the EPM open arms did not overlap with dCA1 OFT center selective neurons above chance levels (Fig. S3H), but were preferentially recruited to an appetitive novel object. This indicates that the dCA1 neurons that are selective for the open arms are

not selective for anxiogenic environments but may rather be responsive to novelty. These results suggest the existence of cells that exhibit stable representations of anxiety-related information or "anxiety cells" that are more abundant in vCA1 than in dCA1.

As our viral targeting strategy could not distinguish between vCA1 pyramidal cells and inhibitory interneurons, we imaged vCA1 inhibitory interneurons to determine whether anxiety cells were overrepresented within this population. We virally expressed a Cre-dependent GCaMP6f in vGAT-Cre mice (Vong et al., 2011) and imaged neural responses in the EPM (Fig. 4A). We found that overall, vCA1-vGAT neurons did not exhibit heightened activity in the open arm compartment (Fig. 4B), but rather that the majority of vCA1-vGAT imaged neurons were closed-arm preferring (Fig. 4C). These results suggest that vCA1 open arm preferring neurons are largely comprised of glutamatergic pyramidal neurons, rather than inhibitory interneurons.

We then assessed whether vCA1 and dCA1 neurons might also differentially represent spatial information. Mice were imaged in the same FOV while exploring two contexts with differing spatial cues (contexts A and B), followed by a second exposure to context A (A-B-A), and rate maps of their firing fields within the contexts were generated as previously described (Leutgeb et al., 2007) (Fig. S4C, S4D). We found that dCA1 neurons encoded more spatial information (Skaggs et al., 1996), and had more stable place fields relative to vCA1, indicating that dCA1 neurons are more spatially tuned than vCA1 (Fig. S4E–H). Taken together, these data suggest that dCA1 is enriched in place cells, while vCA1 is enriched in anxiety cells.

vCA1-Lateral Hypothalamus projection neurons do not significantly overlap with vCA1 projections to the Basal Amygdala or Medial Prefrontal Cortex

Given the heterogeneity of vCA1 responses in the EPM, we next identified through which vCA1 subcortical output streams these effects on anxiety-related behavior could be mediated. We focused on two structures that receive some of the densest vCA1 projections and are known to contribute to anxiety-related behavior, learned fear, and stress responses-the basal amygdala (BA) and lateral hypothalamus (LHA) (Canteras and Swanson, 1992; Cenquizca and Swanson, 2006; Kishi et al., 2006; Tannenholz et al., 2014).

Injection of CaMKII-ChR2-eYFP virus into vCA1 revealed dense terminal labeling in the BA (within the basomedial and basolateral amygdala) and the LHA with similar intensities (Fig. 5A, 5B). Acute slice recordings in BA or LHA neurons in ChR2-eYFP injected mice confirmed monosynaptic input from vCA1 to BA and LHA, as 473nm laser stimulation within BA or LHA subfields was sufficient to elicit glutamatergic, monosynaptic excitatory post synaptic currents (EPSC) (Fig. 5C, 5D).

We next determined whether different populations of vCA1 neurons project to LHA and BA, as recently seen with other outputs to the BLA, CeA, mPFC, lateral septum, and NAc (Cembrowski et al., 2016; Jin and Maren, 2015; Kim and Cho, 2017; Lee et al., 2014b; Okuyama et al., 2016; Parfitt et al., 2017; Xu et al., 2016). Injection of the retrograde tracers cholera toxin subunit B (CTB) CTB-555 and CTB-488 into the BA and LHA, revealed these vCA1 projectors were largely non-overlapping populations, as only ~3% of labeled neurons

sent dual projections (Fig. 5E white arrows, 5F). Interestingly, we also found that BA and LHA projecting neurons were segregated anatomically and organized in a laminar fashion, with vCA1-LHA neurons located deeper in the CA1 pyramidal layer relative to vCA1-BA neurons (Fig. 5G). We next assessed whether vCA1-LHA projecting neurons send collaterals to the Medial Prefrontal Cortex (mPFC)-a pathway that has recently been described to modulate anxiety-related behavior (Padilla-Coreano et al., 2016). We conducted similar retrograde tracing studies as described above and injected CTB-555 into the mPFC and CTB-488 into the LHA, and found that similar to the vCA1-BA pathways, vCA1-LHA projecting neurons were non-overlapping with vCA1-mPFC projecting neurons (Fig. S5A, S5B). Taken together, these studies indicate that vCA1-LHA projecting neurons arise from largely non-overlapping cell populations relative to vCA1-BA and vCA1-mPFC projections, and occupy anatomically distinct layers within vCA1.

vCA1-Amygdala and vCA1-LHA projections differentially contribute to anxiety-related behavior and contextual fear memories

Given the anatomical segregation of vCA1-BA and LHA projections, we next determined if modulation of vCA1-BA and vCA1-LHA projectors differentially contribute to behavior. Mice were injected with ChR2-eYFP or a control eYFP virus into vCA1, and fiber optics were implanted into either the amygdala (targeting the basal nuclei) or LHA (Fig. 6A, 6E; S5F, S5I). Mice were then tested for light effects in tests of anxiety-related behavior and contextual fear conditioning (CFC).

In CFC, mice explored the conditioning context while receiving laser stimulation, after-which they received a brief foot shock. On day two, mice were placed back into the same context in the absence of laser stimulation to test for light effects on CFC encoding. We found that vCA1-amygdala-ChR2 mice froze significantly less than controls, indicating that disrupting normal activity patterns between vCA1-amygdala was sufficient to disrupt encoding of contextual fear (Fig. 6B). To determine whether intact vCA1-BA activity patterns were required for retrieval, a different cohort of mice were trained with light off, and tested for freezing on day two with the light on. vCA1-amygdala-ChR2 mice froze less than controls indicating that vCA1-amygdala activity was required for both encoding and retrieval of contextual fear memory (Fig 6B). These effects were recapitulated with vCA1-amygdala terminal inhibition (Fig. S5C–E), indicating that the effects from ChR2 excitation were likely due to a loss-of-function. Surprisingly, performing the same manipulations in the vCA1- LHA pathway did not impact either the encoding or retrieval of contextual fear, and these negative effects were not frequency specific (Fig. 6F, S5L), indicating a selective role for vCA1- amygdala in context encoding and retrieval.

We next tested the contribution of these vCA1 projections to anxiety-related behavior. While silencing or stimulation of vCA1-amygdala terminals had no effect on percent center distance in the OFT (Fig. 6C, S5C, S5G), stimulation robustly decreased percent center exploration in vCA1-LHA-ChR2 mice- an effect that persisted into the subsequent light off epoch (Fig. 5G). In addition, in an RTPP assay, while stimulation did not produce an effect in vCA1- amygdala-ChR2 mice (Fig. 6D, S5H), stimulation in vCA1-LHA-ChR2 mice elicited avoidance, as vCA1-LHA-ChR2 expressing mice spent significantly less time in the

stimulation chamber relative to controls (Fig. 6H). Importantly, light effects in vCA1-LHA-ChR2 mice were not due to changes in locomotor activity (Fig. S5J & S5K). These studies indicate that modulation of vCA1- LHA, but not vCA1-amygdala projection neurons can impact anxiety-related behaviors and elicit avoidance.

These results support a functional dissociation between vCA1-amygdala and vCA1-LHA neurons, with vCA1-BA projections modulating contextual fear memory encoding and retrieval, and vCA1-LHA neurons driving anxiety-related behavior and aversion.

The vCA1-LHA projection is enriched in anxiety cells

We next investigated whether this functional dissociation was already present at the level of vCA1. A retrograde canine adeno type 2- Cre virus (CAV2-Cre) was injected either into the BA or LHA subfield, and a Cre-dependent GCaMP6f virus was injected into vCA1. A GRIN lens was then implanted over the vCA1 region, and projection-specific Ca^{2+} activity was imaged during identical behavioral conditions as described above (Fig. 7A, 7C). Utilizing this approach, vCA1-GCaMP6f terminals were visualized selectively in BA or LHA subfields, but not in both, confirming projection-specific expression of the Ca^{2+} indicator (Fig. 7B).

Imaging activity in the EPM in the two populations revealed that while both vCA1-BA and vCA1-LHA neurons exhibited increased activity in the open arms (Fig. S6A), the magnitude of the difference between open arm and closed arm activity was greater in vCA1-LHA neurons relative to vCA1-BA projecting neurons (Fig. 7D). In addition, we found that vCA1-LHA neurons were highly enriched in anxiety cells relative to vCA1-BA neurons, with anxiety cells representing 79% of the vCA1-LHA population (Fig. 7E, S6B). Importantly, the groups did not significantly differ in % open arm time and Ca^{2+} activity in the EPM closed arm compartment did not differ between projection- type (Fig. S6A).

We next analyzed the spatial tuning structure and spatial information of the projecting populations as previously described, and found no significant differences between vCA1-BA and vCA1-LHA projection populations (Fig. S6C–G). These studies suggest that while vCA1-LHA projecting neurons are enriched in anxiety-related activity responses relative to vCA1-BA projectors, both projection streams encode low levels of spatial information.

Considering the enrichment of anxiety cells within the vCA1-LHA pathway, we next assessed whether activity in these neurons was necessary for avoidance behavior as previously tested in our whole-population manipulations. We injected CAV2-Cre into the LHA and a Cre-dependent ArchT or control virus into vCA1 and implanted fiber optics into vCA1 (Fig. 7F, S6H). We tested mice in the EPM, and selectively triggered laser stimulation when mice entered the open arm compartment to silence vCA1-LHA anxiety cell activity. We found that silencing vCA1-LHA neurons during open arm exploration significantly reduced avoidance of the open arms, recapitulating the effects we found in our whole-population manipulation (Fig. 7G).

These results support the hypothesis that negative valence information is represented at the level of vCA1, is enriched in neurons projecting to the LHA, and is necessary for avoidance behavior (Fig. S7).

Discussion

A representation of anxiogenic contexts in vCA1

The HPC integrates diverse sensory information from the entorhinal cortex (EC) to generate complex representations of the environment (Canto et al., 2008), which can become paired with aversive stimuli to support contextual fear conditioning (Kim and Fanselow, 1992; Phillips and LeDoux, 1992). In contrast to this purely cognitive view of the HPC, our vCA1 imaging studies indicate that vHPC neurons carry a representation of innately anxiogenic stimuli. We find that vCA1 is enriched in anxiety cells that respond to the open arm compartment of the EPM. Moreover, these neurons are preferentially recruited by other anxiogenic environments, such as the center of the OFT, but not by an appetitive novel object. Further, our closed-loop optogenetic silencing experiments demonstrate that this increase in vCA1 activity in anxiogenic contexts is necessary for the expression of avoidance behavior. Interestingly, we found that vCA1 anxiety cells largely increase their activity after entry into the anxiogenic open arms of the EPM, rather than during the decision point to make that entry (a behavioral condition that has recently been assessed in the vHPC-BLA-mPFC circuit using local field potentials (Jacinto et al., 2016))Therefore, vCA1 may modulate anxiety behaviors by directly encoding threatening stimuli through anxiety cells that are specialized to represent innately anxiogenic environments.

This anxiogenic representation may originate from within the HPC circuit, or may be provided by extra-hippocampal inputs. One such input is the BLA, which projects directly to vCA3 and vCA1, and whose inputs have recently been shown to impact anxiety-related behaviors (Felix-Ortiz et al., 2013). However, this is complicated by single unit recordings, which have shown that BA neurons are preferentially active in the safe closed arm compartment of the EPM, in contrast to vCA1 anxiety cells (Adhikari et al., 2015; Wang et al., 2011). In addition, BLA neurons projecting to vCA1 were found to respond to cues of both positive and negative valence (Beyeler et al., 2016), rather than biasing toward negative valence stimuli as in vCA1 anxiety cells.

Alternatively, this anxiogenic representation in vCA1 could arise via EC inputs that are specialized to recognize specific environmental features that contribute to anxiogenic contexts such as color change, differences in lighting, elevation, and lack of walls (Diehl et al., 2017; Lu et al., 2013). Innate valence representations could thereby arise via selective routing of these features to projection-defined vCA1 populations that modulate avoidance behavior. Thus, future studies recording and controlling input regions will determine the relative contribution of the EC, BLA, and upstream CA3 and dentate gyrus circuits in the generation of the anxiogenic signal in vCA1.

Divergent vCA1 projection streams

It has recently become appreciated that the vCA1 sends parallel and largely non-overlapping projections to the mPFC, lateral septum, NAc, BLA, and central amygdala (Ce) (Cembrowski et al., 2016; Jin and Maren, 2015; Kim and Cho, 2017; Lee et al., 2014b; Okuyama et al., 2016; Parfitt et al., 2017; Xu et al., 2016), and here we find this segregation also within the BA and LHA pathways. Interestingly, in contrast to the intermingled vCA1 projections to the BA and Ce, we found that vCA1-BA and vCA1-LHA projection neurons were organized in a laminar fashion within CA1. Recent studies on CA1 lamination have demonstrated that pyramidal neurons in the deep and superficial layers of CA1 differ in their physiological properties, local inhibitory inputs, and long range inputs (Danielson et al., 2016b; Lee et al., 2014b; Li et al., 2017; Masurkar et al., 2017). Therefore, vCA1-BA and vCA1-LHA projecting neurons may receive different inputs and exhibit different physiological properties, allowing for differential information routing between these populations.

vCA1-LHA as a direct route to control avoidance behavior

Our studies revealed striking pathway-specific control of anxiety-like behavior in vCA1, as activation of vCA1-LHA but not vCA1-BA terminals generates avoidance behavior in anxiety tasks. Moreover, our projection-specific imaging studies showed an enrichment of anxiety cells within the vCA1-LHA projections relative to vCA1-BA projections, with ~80% of the vCA1-LHA population carrying a representation for the open arms of the EPM. The LHA may then integrate this representation from vCA1 with those arising from other areas, such as the BNST, which was found to carry a representation for the closed arms of the EPM, and sends a direct projection to the LHA that produces anxiolytic effects (Kim et al., 2013). Therefore, routing of anxiety representations to the LHA may be critical for the generation of avoidance behaviors. Although we targeted the LHA in our studies, vCA1 sends direct projections to several subnuclei of the hypothalamus (Canteras and Swanson, 1992; Cenquizca and Swanson, 2006), many of which contain diverse cell types and are anatomically challenging to target selectively (Canteras, 2002). Elegant studies have begun to dissect these diverse hypothalamic circuits (Jennings et al., 2013; Jennings et al., 2015; Kunwar et al., 2015; Lee et al., 2014a; Lin et al., 2011; Silva et al., 2013), and future studies investigating the hypothalamic cell-types through which vCA1 and other inputs elicit effects on avoidance behaviors will be critical to understanding how this structure modulates anxiety-like behaviors.

Our studies reveal vCA1 projections to the LHA as a novel pathway by which the vHPC may modulate anxiety-related behavior. Recent studies indicate that vHPC-mPFC projection neurons also represent anxiety-related information in the EPM, and that optogenetic inhibition of vHPC inputs to the mPFC reduces open arm avoidance (Ciocchi et al., 2015; Padilla-Coreano et al., 2016). While glutamatergic cell populations in the LHA may drive rapid avoidance and aversive behaviors directly (Hakvoort Schwerdtfeger and Menard, 2008; Jennings et al., 2013; Kim et al., 2013), the mPFC likely modulates anxiety-related behaviors via outputs to the amygdala, hypothalamus, thalamus, or periaqueductal gray (Do-Monte et al., 2015; Likhtik et al., 2014; Radley et al., 2006; Sesack et al., 1989; Sotres-Bayon and Quirk, 2010). One intriguing possibility is that the contribution of vCA1-LHA

and vCA1-mPFC pathways to anxiety-related behavior is analogous to the thalamic "low road" and cortical "high road" in the control of amygdala-dependent auditory fear conditioning (LeDoux, 1996; LeDoux, 2000). In this model, differential routing of anxiogenic contextual representations between vCA1 pathways could serve a similar function of supporting both a rapid avoidance signal (via enrichment of anxiogenic signals within direct vCA1-LHA projections) and a slower, higher-order representation through cortical integration via the vCA1-mPFC pathway.

vCA1-BA projection neurons mediate learned fear, but not innate avoidance behavior

One interesting aspect of our studies was that fewer anxiety cells were observed in the vCA1-BA population compared to the vCA1-LHA pathway, and manipulating projections from vCA1 to the BA had no impact on innate anxiety tasks, despite studies demonstrating that the reverse pathway (BLA-vHPC) can drive anxiety-like behaviors (Felix-Ortiz et al., 2013). Rather, optogenetic manipulations of the vCA1-BA pathway in our study and other recent work (Xu et al., 2016) demonstrate that this pathway is important in context-fear associations. Therefore, this pathway may be more specialized to encode learned context-valence associations (rather than innately anxiogenic valence representations), whereby contextual input from vCA1 to the BA would become paired with aversive stimuli at the level of BA. Moreover, activity in vCA1-BA anxiety cells may not be sufficient to drive avoidance behavior to innately anxiogenic contexts in the absence of a learned context-fear association.

Our studies raise the intriguing possibility that subpopulations of vCA1 neurons are hardwired to respond to environments that produce innate avoidance, while other populations may be hardwired to respond to environments that elicit approach (Fig. S7). This could be accomplished via selective routing of sensory information to vCA1 populations that can directly drive positive or negative behavioral responses via their segregated limbic target streams. While the vCA1-LHA projectors are enriched in negative valence cells, the vCA1-NAc projectors may be enriched in positive valence cells (Britt et al., 2012; Ciocchi et al., 2015; Okuyama et al., 2016). This model would be similar to that described in the BLA, where distinct subpopulations of neurons respond to positive or negative valence quality (Belova et al., 2007; Gore et al., 2015; Namburi et al., 2015; Paton et al., 2006; Uwano et al., 1995). If vCA1 were organized in a similar fashion, we would predict that single vCA1 neurons would respond to diverse types of sensory stimuli of the same valence to drive analogous behavioral responses. One approach to test this hypothesis will be to assess whether vCA1 anxiety cells also respond to other innately aversive sensory stimuli, such as aversive odors or painful stimuli. Importantly, in the current study we utilized calcium imaging to probe the cellular responses to behaviors that are executed on slow time scales (seconds), which is compatible with the temporal limitations of calcium dynamics. Future, pathway specific single unit electrophysiological recordings both in vHPC and in target regions may elucidate the responses to more rapid anxiety-related behaviors, as well as inform optical stimulation parameters that may recapitulate natural patterns of activity within this circuit and determine the downstream effects of optical stimulation and inhibition.

Our findings provide novel insights into the representation of innately aversive information in the vHPC, and the role of pathway-specific vCA1-subcortical projections in the generation of anxiety-related behavior. The identification of a novel vCA1-LHA circuit that rapidly controls anxiety-related behavior, without impacting learned fear, may provide novel targets for the treatment of mood and anxiety disorders.

Experimental Procedures

CONTACT FOR REAGENTS AND RESOURCE SHARING

Further information and requests for resources and reagents should be directed to and will be fulfilled by the Lead Contact, Rene Hen (rh95@columbia.edu).

EXPERIMENTAL MODELS AND SUBJECT DETAILS

Animal Subjects—All procedures were conducted in accordance with the U.S. NIH Guide for the Care and Use of Laboratory Animals and the New York State Psychiatric Institute Institutional Animal Care and Use Committees at Columbia University. Adult male C57BL/6J mice were supplied by Jackson Laboratory, and Vgat-IRES-Cre mice (Vong et al., 2011) were bred in-house on a C57BL/6J background, and used at 8 weeks of age. Mice were maintained with unrestricted access to food and water on a 12-hour light cycle, and experiments were conducted during the light portion.

Viral Constructs—For optogenetic manipulations, adeno-associated viruses (AAV5-CaMKIIa-hChR2(H134R)- eYFP; AAV5-CaMKIIa-eYFP; AAV5-CaMKII-ArchT-GFP; AAV5-CAG-Flex-ArchT-GFP) were packaged and supplied by the UNC Vector Core Facility at titers of ~4–8 × 10^{12} vg/ml. For calcium imaging, viruses (AAV1-Syn-GCaMP6f.WPRE.SV40; AAV1-Syn-Flex- GCaMP6f.WPRE.SV40) were packaged and supplied by UPenn Vector Core at titers ~6 × 10^{12} vg/ml and viral aliquots were diluted prior to use with artificial cortex buffer to ~2 × 10^{12} vg/ml.

METHOD DETAILS

Stereotactic Surgeries—For all surgical procedures, mice were anesthetized with 1.5% isoflurane at an oxygen flow rate of 1 L/min, and head-fixed in a stereotactic frame (David Kopf, Tujunga, CA). Eyes were lubricated with an ophthalmic ointment, and body temperature maintained at 37°C with a T/pump warm water recirculator (Stryker, Kalamazoo, MI). The fur was shaved and incision site sterilized prior to beginning surgical procedures, and subcutaneous saline and carpofen were provided peri-operatively and for 2 days post-operatively to prevent dehydration and for analgesia.

For in vivo Ca^{2+} imaging, mice underwent a single surgery in which 500nl of GCaMP6f virus was injected unilaterally with a Nanoject syringe (Drummond Scientific, Broomall, PA) prior to implanting a GRIN lens over the injection site. GRIN lenses were implanted with methods previously described (Resendez et al., 2016). Briefly, a craniotomy centered at the lens implantation site was made, and dura was removed from the brain surface and cleaned with a stream of sterile saline and absorptive spears (Fine Science Tools (FST), Foster City, CA) prior to lowering the GRIN lens (no tissue was aspirated out of site). 3 skull

screws (FST, Foster City, CA) were inserted in evenly spaced locations around the implantation site, and the lens was slowly lowered in 0.1 mm DV steps and then fixed to the skull with dental cement (Dentsply Sinora, Philadelphia, PA). For vCA1 imaging, a ~0.5 mm diameter, ~6.1 mm long GRIN lens was used, and for dCA1 a ~1.0 mm diameter, ~4 mm long GRIN lens was used (Inscopix, Palo Alto, CA). Viral injection coordinates were (in mm, from brain tissue at site): (vCA1: −3.16 AP, 3.25 ML, −3.85, −3.50, −3.25 DV; dCA1: −2.15 AP, 1.85 ML, −1.55, −1.65 DV) and lens coordinates were (in mm, from skull at craniotomy): (vCA1: −3.16 AP, 3.50 ML, −3.50 DV; dCA1: −2.15 AP, 1.30 ML, −1.30 DV). At the completion of surgery, the lens was protected with liquid mold rubber (Smooth-On, Lower Macungie, PA), and imaging experiments commenced 3 weeks later.

For optogenetic surgeries, mice underwent a single surgery in which 500nl of opsin virus was injected into the vCA1 subregion with a Nanoject syringe as described above, prior to implanting fiber optics at the target site. Fiber optics were made with procedures previously published (Kheirbek et al., 2013), and were cut at ~5mm in length for implantation. A single skull screw was implanted to allow for better adherence of the dental cement to the skull surface. Virus was injected in vCA1 at the following coordinates for all optogenetic manipulations (in mm): (−3.16 AP, 3.30 ML, −3.85, −3.50, −3.00 DV from brain at craniotomy). vCA1 cell body silencing was done with bilateral virus and fiber optic implantation at the following coordinates (in mm): (−3.20 AP, 3.35 ML, −3.50 DV from brain at craniotomy). vCA1-BA terminal activation was done bilaterally with fiber optic implantation at (in mm, from brain at craniotomy): (−1.70 AP, 3.00 ML, −4.00 DV), and vCA1-LHA was done with unilateral virus and fiber optic implanted at: (−1.95 AP, 0.50 ML, −4.75 DV). vCA1-LHA-ArchT cell body silencing surgeries were done bilaterally with CAV2-Cre injection into LHA at the above coordinates. For vCA1 cell body silencing, mice were allowed to recover for 4 weeks prior to commencing behavior experiments. For terminal activation, experiments began 8 weeks after surgery to allow for sufficient viral expression and trafficking of opsin to axon terminals.

For CTB retrograde studies, 290nl of conjugated CTB (Life Technologies, Carlsbad, CA) was injected unilaterally in the LHA and BA subregions or LHA and mPFC in a single surgery at the following coordinates (in mm from brain tissue at site): (LH: −2.0 AP, 0.75 ML, −5.25, −5.0, −4.75 DV; BA: −1.70 AP, 3.0 ML, −4.25, −4.0 DV; mPFC: +1.90 AP, 0.3 ML, −2.75, −2.50 DV), and mice were perfused 7 days after injection for histology.

Patch-Clamp Electrophysiology—For vCA1-ChR2 terminal slice recordings, mice with vCA1 viral expression of the excitatory ChR2-eYFP opsin (at 8 weeks post viral injection, to allow for trafficking of opsin to axon terminals) were anesthetized by halothane or isoflurane inhalation, decapitated, and brains rapidly removed. Coronal slices (350 μm) containing the BA and LHA were cut on a Leica VT1000S vibratome in ice cold partial sucrose artificial cerebrospinal fluid (ACSF) solution containing (in mM): 80 NaCl, 3.5 KCl, 4.5 $MgSO_4$, 0.5 $CaCl_2$, 1.25 H_2PO_4, 25 $NaHCO_3$, 10 glucose, and 90 sucrose equilibrated with 95% O_2/ 5% CO_2 and stored in the same solution at 37°C for 30 minutes, then at room temperature until use. Recordings were made at 30–32°C (TC324-B; Warner Instrument Corp) in ACSF (in mM: 124 NaCl, 2.5 KCl, 1 NaH_2PO_4, 25 $NaHCO_3$, 20 glucose, 1 $MgCl_2$, 2 $CaCl_2$). Fluorescent vCA1-ChR2-eYFP axon terminals were first located within the BA

and LHA on an upright microscope Axioskop-2 FS (Zeiss). Cells surrounded by these axons were then visualized via infrared-differential interference contrast (IR-DIC) optics and randomly selected for voltage-clamp recordings. A cesium-based internal solution was used (in mM): 125 Cs-methanesulfonate, 4 NaCl, 10 HEPES, 1 EGTA, 4 MgATP, 0.3 Na_2GTP, 10 Na-phosphocreatine, 5 QX 314-Cl). Patch pipettes were made from borosiliate glass (A-M Systems) using a micropipette puller (Model P-1000; Sutter Instruments). In the bath, initial pipette resistance was 4.5-6.5 MΩ. Recordings were made without correction for junction potentials. Current and voltage signals were recorded with a MultiClamp 700B amplifier (Molecular Devices, USA), digitized at 5–10 kHz, and filtered at 2.5– 4 kHz. Data were acquired and analyzed using Axograph (Axograph Scientific, Sydney, Australia).

For optical stimulation, 473 nm light pulses were generated using a 100 mW DPSS laser (Opto Engine LLC, Midvale, UT) and delivered through a 40X objective. Single light pulses (1 ms duration) delivered every 20 sec were used to activate vCA1 fibers in the BA and LHA while recording light-evoked monosynaptic EPSCs in randomly chosen neurons.

For vCA1-ArchT cell body slice recordings, mice with ArchT expression (4 weeks post viral injection) were anesthetized and perfused with modified sucrose ACSF containing (in mM) 75 NaCl, 2.5 KCl, 3.3 $MgSO_4$, 0.5 $CaCl_2$, $1NaH_2PO_4$, 26.2 $NaHCO_3$, 22 glucose, 52.6 sucrose, 10 HEPES, 10 choline chloride, 1 pyruvate, 1 L-ascorbic acid (~300 mOsml, pH 7.4). The brain was dissected and 300 μm-thick slices were cut and placed in an interface chamber containing the same modified sucrose solution. Slices were incubated at 32° C for 30 min, then held at room temperature (23° C) in the interf ace chamber for at least 1 h. Recordings were made at room temperature and perfused with oxygenated ACSF containing (in mM) 119 NaCl, 2.5 KCl,1.3 $MgCl_2$, 2.5 $CaCl_2$, 1.3 NaH_2PO_4, 26.0 $NaHCO_3$, 20 glucose (~300 mOsml) at 23°C.

Recordings were made at room temperature using pulled patch pipettes (5-7 MΩ) filled with internal solution containing (in mM) 150 K-Gluconate, 1.5 $MgCl_2$, 5.0 HEPES, 1 EGTA, 10 phosphocreatine, 2.0 ATP, and 0.3 GTP. Green light was supplied via an arc lamp passed through a TRITC excitation filter, and delivered through a 40× objective centered on the soma of the patched cell. Patch-clamp recordings were obtained using Multiclamp 700B patch amplifiers, digitized using a Digidata 1322a, and data collected using pClamp 10 software (Molecular Devices).

Behavioral Assays

Elevated Plus Maze: Mice were placed in a standard EPM sized maze (13.5″ height of maze from floor, 25″ full length of each arm-type, 2″ arm width, 7″ tall closed arms, with 0.5″ tall/wide ledges on the open arms), with ~650 light lux centered over the open arms to promote avoidance. Mice were placed in the center region of the maze, and were allowed to explore for 10 minutes while recording behavior with a webcam EthoVision XT 10 (Noldus, Leesburg, VA) or a digital camera (Carl Zeiss), and analyzed with EthoVision software or TopScan tracking software (Clever Sys, Reston, VA). Headdip behaviors in the EPM were hand-scored with Observer XT software (Noldus, Leesburg, VA). For ArchT-GFP silencing experiments, mice were run for 20 minutes in the EPM to allow for a sufficient number of open arm entries/ laser triggering events.

Novel Object task: Mice were placed in a familiar arena ($22 \times 16 \times 6''$ length-width-height) which they were allowed to explore for 20 minutes on the previous day, in low light lux condition (~50 lux). Behavior during the initial exposure to the arena was recorded and tracked with EthoVision XT 10 software, and 4 corner zones of equal size were drawn to determine the relative baseline preference for each location (~$6 \times 5.5''$ length-width). During the novel object session, a novel object that elicited approach (a funnel taped down with colored tape) was placed into the least preferred corner zone of the arena (from day 1 tracking). Mice were allowed to explore the familiar arena for 10 minutes and behavior was recorded with EthoVision XT 10 software and webcam.

Open Field Test: Mice were placed in an arena ($18 \times 18 \times 12''$ length-width-height; Kinder Scientific, Poway, CA) with bright light (~650 lux) centered over the center zone, and allowed to explore for 10 minutes while behavior was recorded and analyzed with MotorMonitor software.

Context exploration task for place field analysis: For place field analysis, mice were allowed to explore a novel arena (Context A- Context B-and Context A) ($9.5 \times 18''$ length-width) for 10 minutes each in low light lux conditions, with a 10 minute rest in a transfer cage in between sessions. Context A was a plain arena with short walls ($6''$ height) while Context B was generated by placing standard mouse bedding, and tall, rounded yellow walls ($10''$ height) within the same arena as Context A. The arena was kept in the same location for all 3 imaging sessions, and behavior was recorded and tracked with EthoVision XT 10 software.

Real-Time Place Preference: Mice were placed in an identical 2-chamber arena ($18.5 \times 10 \times 8''$ length-width-height) with standard mouse bedding and low light lux, and allowed to freely explore both chambers for 20 minutes while behavior was recorded with EthoVision XT 10 software.

Contextual Fear conditioning: Mice were run through a 2-day contextual fear conditioning paradigm. On day 1, mice were placed in a standard fear conditioning shock box (Coulbourn Instruments, Holliston, MA) with the following contextual cues: (anise scent, white noise, and a light on within the chamber), and were allowed to explore the context for 3 minutes prior to receiving a 2 second 0.7mA strength foot shock. On day 2, mice were placed back into the same context for 3 minutes to assess for freezing during CFC retrieval. For vCA1-LHA terminal modulation, at the end of day 2 retrieval, mice were given an additional 2 second foot shock to re-train them for day 3 retrieval testing. Behavior was recording with FreezeFrame video software (Coulbourn Instruments, Holliston, MA), and freezing was hand-scored by a blinded experimenter using Stopwatch scoring software (Center for Behavioral Neuroscience).

Freely Moving Ca^{2+} imaging—3 weeks after surgery, mice were checked for GCaMP expression with a miniaturized microscope (Inscopix, Palo Alto, CA) and procedures previously described (Resendez et al., 2016). Mice were briefly anesthetized with 1.5% isoflurane at 1 L/min oxygen flow, and head-fixed into a stereotactic frame. The protective rubber mold was removed from the lens, and a magnetic baseplate was attached to a

microscope and lowered over the implanted GRIN lens to assess the FOV for GCaMP+ neurons. If GCaMP+ neurons were visible, the baseplate was dental cemented in place onto the mouse headcap to allow for re-imaging of the same FOV for several weeks. Once baseplated, the same microscope was used for every imaging session with that mouse, and the focal plane on the hardware of the miniscope was not altered throughout the imaging experiments to ensure a constant FOV across sessions. Awake- behaving imaging sessions were commenced the day after baseplating, and mice were briefly anesthetized (<5mins) in order to attach the miniscope to the baseplate each imaging session day. Mice were allowed to recover from anesthesia for 30 minutes before beginning imaging.

Ca^{2+} videos were recorded with nVista acquisition software (Inscopix, Palo Alto, CA), and triggered with a TTL pulse from EthoVision XT 10 and Noldus IO box system to allow for simultaneous acquisition of Ca^{2+} and behavioral videos. Ca^{2+} videos were acquired at 15 frames per second with 66.56 ms exposure. An optimal LED power was selected for each mouse based on GCaMP expression in the FOV (pixel values), and the same LED settings were used for each mouse throughout the series of imaging sessions.

Optogenetic Manipulations—Mice were handled and habituated to fiber optic adaptor cables for 3 days prior to commencing behavioral experiments. For ArchT-GFP silencing experiments, ~10mW of constant light were delivered via a 523nm 100mW laser (Opto Engine, Midvale, UT; a 594nm laser was used in vCA1-BA Arch silencing experiments) to fiber optics implanted in mouse brain using a fiber optic patch cable as previously described (Kheirbek et al., 2013). For ChR2-eYFP experiments, ~5-8mW of 5ms 10hz or 20hz light pulses were delivered via a 473nm 100mW laser (Opto Engine, Midvale, UT), and light delivery protocol was controlled via a Master-8 stimulator (AMPI, Jerusalem, Israel). For closed-loop ArchT-GFP silencing experiments, EthoVision XT 10 software and Noldus IO box system were used to record live- tracking of mice while they explored the EPM, OFT, and RTPP tasks. The laser was triggered- ON when mice were live-tracked in EthoVision in a pre-drawn stimulation zone (open arms for EPM, center for OFT, and a randomly selected chamber for RTPP). For ChR2-eYFP experiments, OFT optogenetic manipulations were ran in 3 minute laser epochs (light on-off-on). RTPP was ran as described above. In CFC, on light-ON days, light was delivered for the entire session (including through the end of the foot shock on day 1 light-ON cohorts).

Histology and Confocal and Epifluorescent Microscopy—For all histology, mice were perfused transcardially with 4% (weight/volume) paraformaldehyde in 1X phosphate buffer solution (PBS) and brains were then removed and post-fixed in 4% PFA for 24 hours, after-which they were transferred to a 30% sucrose solution in PBS for 2 days. Sucrose-saturated brains were then flash-frozen and sliced in 50um thick coronal sections on a cryostat (Leica CM 3050S). Sections were incubated with 1:1000 Hoechst in $1\times$ PBS (Invitrogen, Carlsbad, CA) for 10 minutes to label cell nuclei, and mounted and cover-slipped with ProLong Gold antifade reagent (Invitrogen, Carlsbad, CA). Endogenous viral expression of fluorophores was used in all histology preparations (no immunolabeling was required to visualize fluorophores). Histology slides were imaged on a (Leica TCS SP8)

confocal microscope using a 10× or 20× objective, or a (Zeiss Axiovert 200) epifluorescent microscope using a 2.5× or 10× objective.

Appropriate GRIN lens and fiber optic placements were determined by post-fixing brains with head-caps and skulls intact for 1 week in 4% PFA to improve the clarity of the GRIN lens and fiber optic tracts. Brains were then placed into 30% sucrose solution as described above, and slices were collected in individual culture wells to maintain the accurate AP order of sections for fiber optic/lens placement reconstructions. Sections were then mounted in AP order, and the bottom location of fiber optic tips and GRIN lenses were visually determined for each mouse by inspecting sections on an epifluorescent microscope.

For CTB retrograde studies, tiled images were captured on a confocal microscope with a 10× objective, and red, green, and yellow cells were counted with an ImageJ Cell Counter toolbox. Lamination of CTB labeled neurons was determined by measuring the distance of counted cells to the Pyr/Rad border in ImageJ.

For anterograde terminal fluorescence measurements, the vCA1 terminal fields in the BA and LHA were visualized in the same AP location (−1.70 mm) in vCA1-ChR2-eYFP expressing mice (8 weeks post-viral injection to allow for sufficient trafficking of opsin to axon terminals). The BA and LHA subfields were then imaged in the same section with identical exposure times using a 2.5× objective on an upright epifluorescent microscope. This allowed us to control for differences in baseline background fluorescence between sections, as BA and LHA terminal images were taken from the same sections, and fluorescence levels compared in a pair-wise fashion. ROIs of the BA and LHA were hand-drawn in ImageJ, and the mean fluorescence value was used for comparisons.

Image Processing—For whole-population (Synapsin promoter) imaging, image processing was performed using Mosaic software (version 1.0.5b; Inscopix, Palo Alto, CA). Videos were spatially downsampled by a binning factor of 4 (16×), and lateral brain movement was motion corrected using the registration engine Turboreg (Ghosh et al., 2011; Ziv et al., 2013) which utilizes a single reference frame and high-contrast features in the image to shift frames with motion to matching XY positions throughout the video. Black borders from XY translation in motion correction were cropped, and changes in fluorescence were detected by generating a F/F_o video using a minimum z-projection image of the entire movie as the reference F_o to normalize fluorescence signals to the minimum fluorescence of pixels within the frame. Videos were then temporally downsampled by a binning factor of 3 (down to 5 frames per second). Putative single cells and Ca^{2+} signals were isolated with an automated cell-segmentation algorithm that employs independent and principal component analyses on F/F_o videos (Mukamel et al., 2009). Identified putative cells were then sorted via visual inspection to select for units with the appropriate spatial configuration and Ca^{2+} dynamics consistent with signals from individual neurons. Ca^{2+} transient events were then defined by a Ca^{2+} event detection algorithm which identifies large amplitude peaks with fast rise times and exponential decays (parameters: tau=200ms, Ca^{2+} transient event minimum size= 6 median average deviation).

For projection-specific imaging, videos were spatially binned, motion corrected and cropped using Mosaic software in an identical fashion as described above, however cell segmentation was performed using an improved automated algorithm optimized for microendoscopic Ca^{2+} imaging- Constrained Non-negative Matrix Factorization for microEndoscopic data (CNMF-E) (Zhou, 2016). CNMF-E builds on a constrained nonnegative matrix factorization (NMF) framework (Pnevmatikakis et al., 2016), and is capable of achieving simultaneous denoising, deconvolution, and demixing of this imaging data. At a technical level, it utilizes a novel model to efficiently estimate and subtract the large background signals present in the data (details of the method can be found in (Zhou, 2016)). Motion corrected and cropped videos were ran through the CNMF-E algorithm with an estimated cell diameter of 18 pixels (measured on visible cells in imageJ). Putative neurons were identified, and sorted by visible inspection for appropriate spatial configuration and Ca^{2+} dynamics as described above, and putative units were manually merged or split if the spatial configuration did not match regions of interests (ROI) manually drawn in ImageJ ROI manager from visual inspection of a $\Delta F/F_o$ version of the video. In the paper, we report the non-denoised temporal traces extracted by CNMF-E as neurons' temporal activity. These traces were z-scaled with an estimated Gaussian noise level, corresponding to a scaled version of $\Delta F/F_o$ of each neuron. Ca^{2+} transient events were then defined with an event detection algorithm similar to that described above. Transients were Z-scored with the mean calculated from time points lacking Ca^{2+} activity (defined as time points with fluorescence values less than the 0.50 quantile of all fluorescence values from all cells in the FOV). Ca^{2+} events were then defined as transients exceeding a 2 s.d. amplitude from a 0.5 s.d. baseline, lasting a minimum duration (calculated by $[-ln(A/Ao)/t\_half]$ where Ao=0.5 and A= amplitude of that transient; t_half for GCaMP6f was 200ms, taken from (Chen et al., 2013)) before returning to a 0.5 s.d. baseline level. Additional Ca^{2+} transient rising events within detected Ca^{2+} transients that were large and mult-peaked were then detected using the findpeaks function in MATLAB (Mathworks, Natick, MA) with the following parameters (MinPeakProminence=1.5 s.d., MinPeakDistance= 1 sec). All detected Ca^{2+} transients were visibly inspected for each cell to verify accuracy. Area under the curve was calculated for identified transients from transient onset (at time when transient exceeded 0.5 s.d. threshold) to offset (at time when transient amplitude returned to 0.5 s.d. baseline threshold).

For tracking cells across multiple imaging session days, videos from multiple sessions were concatenated into a single large video, and motion correction was ran on the concatenated video from a single reference frame to ensure that XY translation from the TurboReg motion correction algorithm adjusted all frames to the same location. Motion correction accuracy on the concatenated video was then determined by visually tracking multiple cells in the FOV across imaging sessions to ensure that cells did not shift their spatial location (from a hand-drawn ROI in ImageJ ROI Manager) throughout the entire length of the video. The accuracy of cell tracking and spatial stability across imaging days in the segmented concatenated video was then quantified in analysis described in Supplementary Figure S3A–E. Briefly (expanding on the detailed description in the figure legend for S3A–E), the Ca^{2+} transient temporal correlation threshold for identifying temporally matched pairs between concatenated video and single video cell segmentation groups was selected by visual inspection of the overlaid Ca^{2+} transients between cell pairs with maximum correlation

(each cell was assigned a putative match to the cell in the second video with which its transient correlation value was maximal). This resulted in a bimodal distribution of cell pair temporal correlations, with a split at Rho=0.4 (all cell pairs with transients exceeding 0.4 correlation were then considered a match).

QUANTIFICATION AND STATISTICAL ANALYSIS

All statistical parameters for specific analyses are reported in the figure legends of the paper.

Ca^{2+} Data Analysis—Ca^{2+} transient events and mouse behavior were analyzed with custom MATLAB (Mathworks, Natick, MA) functions to calculate the rate of Ca^{2+} transients per cell while mice explored different zones, and different XY spatial locations of the arena. Occupancy in different arena zones were defined in EthoVision software and exported as a logical output at 30 frames per second (xy location of the mouse center-point was tracked in the Ethovision-defined arena to categorize behavioral samples into specific arena zones). For headdip behavior scoring, Observer XT software (Noldus, Leesburg, VA) was used to hand-score headdip events and then exported as a logical output similar to the zone behavior tracking described above (a hold-key scoring system was used to log the timing of headdip events throughout the duration of the session). Behavior data was downsampled to 5 frames per second to match Ca^{2+} transient data sampling, and Ca^{2+} transient time bins were categorized into arena zones based on the time-matched Ethovision behavior output to calculate the AUC and rate of Ca^{2+} transients in different behavioral conditions.

For plotting example raster Ca^{2+} heatmaps by distance of vCA1 activity in the EPM, the xy displacement of the mouse center-point (from Ethovision tracking) from the EPM arena center-point was calculated from each behavioral time bin, and xy displacements were categorized by arm-type, and binned by distance (0.5cm bins). The mean Ca^{2+} transient activity (from identified Ca^{2+} transients only) within each behavioral xy displacement bin was then calculated and normalized for each cell individually. For Ca^{2+} heatmaps by time, the mean Ca^{2+} transient activity across all cells in a FOV was calculated in 200ms time bins.

For defining cell selectivity, Ca^{2+} events were shuffled in time for individual cells (1000 iterations), and shuffled rates were re-calculated based on behavior zone time bin categorization as described above (behavior time bins kept constant) to generate a null distribution of zone Ca^{2+} event rates for each cell. A cell was considered selective for a zone if its Ca^{2+} event rate difference between zones (EPM: open-closed; OFT: center-periphery; Novel Object: Novel Object Zone- Neutral Zone) exceeded a 1SD threshold from the null distribution (threshold was determined by comparing zone rates for "neutral cells" defined at different thresholds, and the threshold at which neutral cells showed no significant Ca^{2+} transient rate different between zones was selected).

Place cell analysis—Place field maps were drawn as previously described (Leutgeb et al., 2007) with a bin size of ~5cm^2, and a sigma smoothing factor of 5, drawn from mobile time bins only (immobile time bins were defined as velocities< 1cm/sec, for behavioral bouts>1 sec duration). A minimum of 10 Ca^{2+} transient events in the session was required to be included in the analysis, and qualified place fields were defined as place fields with 9

contiguous bins containing 20% of the peak firing rate. Spatial information content values were calculated from the first context-A exposure imaging session. Spatial information p-values were calculated as previously described (Danielson et al., 2016a) by generating a null distribution of spatial information content values per cell (shuffling the timing of Ca^{2+} events in time to generate null place field maps, 1000 iterations), and comparing the true spatial information content value to that shuffled distribution. Place field stability was determined by comparing the R value from place field map correlations (Pearson's correlation). Only cells with qualified place fields in both conditions (A-A, or A-B) were included in this analysis.

Task-selectivity analysis—To define task-selective neurons, cells were defined by their selectivity for the EPM open arm, OFT center zone, and Novel Object zone as described above. Populations of selective cells were then compared. Overlap significance was determined by randomly sampling from a mock distribution of cells containing the true % of EPM open arm cells in the population (sampling N= total number of OFT center of Novel Object cells, mock distribution N= total number of all cells included in the analysis, sampling at 10,000 iterations), to generate an overlap distribution by random sampling. The true overlap p-value was then calculated by comparing the true overlap value to these distributions.

Supplementary Material

Refer to Web version on PubMed Central for supplementary material.

Acknowledgments

References

Adhikari A, Lerner TN, Finkelstein J, Pak S, Jennings JH, Davidson TJ, Ferenczi E, Gunaydin LA, Mirzabekov JJ, Ye L, et al. Basomedial amygdala mediates top-down control of anxiety and fear. Nature. 2015; 527:179–185. [PubMed: 26536109]

Bannerman DM, Deacon RM, Offen S, Friswell J, Grubb M, Rawlins JN. Double dissociation of function within the hippocampus: spatial memory and hyponeophagia. Behav Neurosci. 2002; 116:884–901. [PubMed: 12369808]

Belova MA, Paton JJ, Morrison SE, Salzman CD. Expectation modulates neural responses to pleasant and aversive stimuli in primate amygdala. Neuron. 2007; 55:970–984. [PubMed: 17880899]

Beyeler A, Namburi P, Glober GF, Simonnet C, Calhoon GG, Conyers GF, Luck R, Wildes CP, Tye KM. Divergent Routing of Positive and Negative Information from the Amygdala during Memory Retrieval. Neuron. 2016; 90:348–361. [PubMed: 27041499]

Britt JP, Benalioaud F, McDevitt RA, Stuber GD, Wise RA, Bonci A. Synaptic and behavioral profile of multiple glutamatergic inputs to the nucleus accumbens. Neuron. 2012; 76:790–803. [PubMed: 23177963]

Calhoon GG, Tye KM. Resolving the neural circuits of anxiety. Nat Neurosci. 2015; 18:1394–1404. [PubMed: 26404714]

Canteras NS. The medial hypothalamic defensive system: hodological organization and functional implications. Pharmacol Biochem Behav. 2002; 71:481–491. [PubMed: 11830182]

Canteras NS, Swanson LW. Projections of the ventral subiculum to the amygdala, septum, and hypothalamus: a PHAL anterograde tract-tracing study in the rat. J Comp Neurol. 1992; 324:180–194. [PubMed: 1430328]

Canto CB, Wouterlood FG, Witter MP. What does the anatomical organization of the entorhinal cortex tell us? Neural Plast. 2008; 2008:381243. [PubMed: 18769556]

Cembrowski MS, Wang L, Sugino K, Shields BC, Spruston N. Hipposeq: a comprehensive RNA-seq database of gene expression in hippocampal principal neurons. Elife. 2016; 5:e14997. [PubMed: 27113915]

Cenquizca LA, Swanson LW. Analysis of direct hippocampal cortical field CA1 axonal projections to diencephalon in the rat. J Comp Neurol. 2006; 497:101–114. [PubMed: 16680763]

Cenquizca LA, Swanson LW. Spatial organization of direct hippocampal field CA1 axonal projections to the rest of the cerebral cortex. Brain Res Rev. 2007; 56:1–26. [PubMed: 17559940]

Chen TW, Wardill TJ, Sun Y, Pulver SR, Renninger SL, Baohan A, Schreiter ER, Kerr RA, Orger MB, Jayaraman V, et al. Ultrasensitive fluorescent proteins for imaging neuronal activity. Nature. 2013; 499:295–300. [PubMed: 23868258]

Ciocchi S, Passecker J, Malagon-Vina H, Mikus N, Klausberger T. Brain computation. Selective information routing by ventral hippocampal CA1 projection neurons. Science. 2015; 348:560–563. [PubMed: 25931556]

Danielson NB, Kaifosh P, Zaremba JD, Lovett-Barron M, Tsai J, Denny CA, Balough EM, Goldberg AR, Drew LJ, Hen R, et al. Distinct Contribution of Adult-Born Hippocampal Granule Cells to Context Encoding. Neuron. 2016a; 90:101–112. [PubMed: 26971949]

Danielson NB, Zaremba JD, Kaifosh P, Bowler J, Ladow M, Losonczy A. Sublayer-Specific Coding Dynamics during Spatial Navigation and Learning in Hippocampal Area CA1. Neuron. 2016b; 91:652–665. [PubMed: 27397517]

Diehl GW, Hon OJ, Leutgeb S, Leutgeb JK. Grid and Nongrid Cells in Medial Entorhinal Cortex Represent Spatial Location and Environmental Features with Complementary Coding Schemes. Neuron. 2017

Do-Monte FH, Quinones-Laracuente K, Quirk GJ. A temporal shift in the circuits mediating retrieval of fear memory. Nature. 2015; 519:460–463. [PubMed: 25600268]

Fanselow MS, Dong HW. Are the dorsal and ventral hippocampus functionally distinct structures? Neuron. 2010; 65:7–19. [PubMed: 20152109]

Felix-Ortiz AC, Beyeler A, Seo C, Leppla CA, Wildes CP, Tye KM. BLA to vHPC inputs modulate anxiety-related behaviors. Neuron. 2013; 79:658–664. [PubMed: 23972595]

Ghosh KK, Burns LD, Cocker ED, Nimmerjahn A, Ziv Y, Gamal AE, Schnitzer MJ. Miniaturized integration of a fluorescence microscope. Nat Methods. 2011; 8:871–878. [PubMed: 21909102]

Gore F, Schwartz EC, Brangers BC, Aladi S, Stujenske JM, Likhtik E, Russo MJ, Gordon JA, Salzman CD, Axel R. Neural Representations of Unconditioned Stimuli in Basolateral Amygdala Mediate Innate and Learned Responses. Cell. 2015; 162:134–145. [PubMed: 26140594]

Hakvoort Schwerdtfeger RM, Menard JL. The lateral hypothalamus and anterior hypothalamic nucleus differentially contribute to rats' defensive responses in the elevated plus-maze and shock-probe burying tests. Physiol Behav. 2008; 93:697–705. [PubMed: 18164736]

Jacinto LR, Cerqueira JJ, Sousa N. Patterns of Theta Activity in Limbic Anxiety Circuit Preceding Exploratory Behavior in Approach-Avoidance Conflict. Front Behav Neurosci. 2016; 10:171. [PubMed: 27713693]

Jacobson L, Sapolsky R. The role of the hippocampus in feedback regulation of the hypothalamic-pituitary-adrenocortical axis. Endocr Rev. 1991; 12:118–134. [PubMed: 2070776]

Jennings JH, Rizzi G, Stamatakis AM, Ung RL, Stuber GD. The inhibitory circuit architecture of the lateral hypothalamus orchestrates feeding. Science. 2013; 341:1517–1521. [PubMed: 24072922]

Jennings JH, Ung RL, Resendez SL, Stamatakis AM, Taylor JG, Huang J, Veleta K, Kantak PA, Aita M, Shilling-Scrivo K, et al. Visualizing hypothalamic network dynamics for appetitive and consummatory behaviors. Cell. 2015; 160:516–527. [PubMed: 25635459]

Jin J, Maren S. Fear renewal preferentially activates ventral hippocampal neurons projecting to both amygdala and prefrontal cortex in rats. Sci Rep. 2015; 5:8388. [PubMed: 25669753]

Jovanovic T, Ressler KJ. How the neurocircuitry and genetics of fear inhibition may inform our understanding of PTSD. Am J Psychiatry. 2010; 167:648–662. [PubMed: 20231322]

Jung MW, Wiener SI, McNaughton BL. Comparison of spatial firing characteristics of units in dorsal and ventral hippocampus of the rat. J Neurosci. 1994; 14:7347–7356. [PubMed: 7996180]

Keinath AT, Wang ME, Wann EG, Yuan RK, Dudman JT, Muzzio IA. Precise spatial coding is preserved along the longitudinal hippocampal axis. Hippocampus. 2014; 24:1533–1548. [PubMed: 25045084]

Kheirbek MA, Drew LJ, Burghardt NS, Costantini DO, Tannenholz L, Ahmari SE, Zeng H, Fenton AA, Hen R. Differential control of learning and anxiety along the dorsoventral axis of the dentate gyrus. Neuron. 2013; 77:955–968. [PubMed: 23473324]

Kheirbek MA, Klemenhagen KC, Sahay A, Hen R. Neurogenesis and generalization: a new approach to stratify and treat anxiety disorders. Nat Neurosci. 2012; 15:1613–1620. [PubMed: 23187693]

Kim JJ, Fanselow MS. Modality-specific retrograde amnesia of fear. Science. 1992; 256:675–677. [PubMed: 1585183]

Kim SY, Adhikari A, Lee SY, Marshel JH, Kim CK, Mallory CS, Lo M, Pak S, Mattis J, Lim BK, et al. Diverging neural pathways assemble a behavioural state from separable features in anxiety. Nature. 2013; 496:219–223. [PubMed: 23515158]

Kim WB, Cho JH. Synaptic Targeting of Double-Projecting Ventral CA1 Hippocampal Neurons to the Medial Prefrontal Cortex and Basal Amygdala. J Neurosci. 2017

Kishi T, Tsumori T, Yokota S, Yasui Y. Topographical projection from the hippocampal formation to the amygdala: a combined anterograde and retrograde tracing study in the rat. J Comp Neurol. 2006; 496:349–368. [PubMed: 16566004]

Kjaerby C, Athilingam J, Robinson SE, Iafrati J, Sohal VS. Serotonin 1B Receptors Regulate Prefrontal Function by Gating Callosal and Hippocampal Inputs. Cell Rep. 2016; 17:2882–2890. [PubMed: 27974203]

Kjelstrup KG, Tuvnes FA, Steffenach HA, Murison R, Moser EI, Moser MB. Reduced fear expression after lesions of the ventral hippocampus. Proc Natl Acad Sci U S A. 2002; 99:10825–10830. [PubMed: 12149439]

Kunwar PS, Zelikowsky M, Remedios R, Cai H, Yilmaz M, Meister M, Anderson DJ. Ventromedial hypothalamic neurons control a defensive emotion state. Elife. 2015; 4

LeDoux, JE. The emotional brain : the mysterious underpinnings of emotional life. (New York: Simon & Schuster); 1996.

LeDoux JE. Emotion circuits in the brain. Annu Rev Neurosci. 2000; 23:155–184. [PubMed: 10845062]

Lee H, Kim DW, Remedios R, Anthony TE, Chang A, Madisen L, Zeng H, Anderson DJ. Scalable control of mounting and attack by Esr1+ neurons in the ventromedial hypothalamus. Nature. 2014a; 509:627–632. [PubMed: 24739975]

Lee SH, Marchionni I, Bezaire M, Varga C, Danielson N, Lovett-Barron M, Losonczy A, Soltesz I. Parvalbumin-positive basket cells differentiate among hippocampal pyramidal cells. Neuron. 2014b; 82:1129–1144. [PubMed: 24836505]

Leutgeb JK, Leutgeb S, Moser MB, Moser EI. Pattern separation in the dentate gyrus and CA3 of the hippocampus. Science. 2007; 315:961–966. [PubMed: 17303747]

Li Y, Xu J, Liu Y, Zhu J, Liu N, Zeng W, Huang N, Rasch MJ, Jiang H, Gu X, et al. A distinct entorhinal cortex to hippocampal CA1 direct circuit for olfactory associative learning. Nat Neurosci. 2017; 20:559–570. [PubMed: 28263300]

Likhtik E, Stujenske JM, Topiwala MA, Harris AZ, Gordon JA. Prefrontal entrainment of amygdala activity signals safety in learned fear and innate anxiety. Nat Neurosci. 2014; 17:106–113. [PubMed: 24241397]

Lin D, Boyle MP, Dollar P, Lee H, Lein ES, Perona P, Anderson DJ. Functional identification of an aggression locus in the mouse hypothalamus. Nature. 2011; 470:221–226. [PubMed: 21307935]

Lu L, Leutgeb JK, Tsao A, Henriksen EJ, Leutgeb S, Barnes CA, Witter MP, Moser MB, Moser EI. Impaired hippocampal rate coding after lesions of the lateral entorhinal cortex. Nat Neurosci. 2013; 16:1085–1093. [PubMed: 23852116]

Masurkar AV, Srinivas KV, Brann DH, Warren R, Lowes DC, Siegelbaum SA. Medial and Lateral Entorhinal Cortex Differentially Excite Deep versus Superficial CA1 Pyramidal Neurons. Cell Rep. 2017; 18:148–160. [PubMed: 28052245]

Moser MB, Moser EI, Forrest E, Andersen P, Morris RG. Spatial learning with a minislab in the dorsal hippocampus. Proc Natl Acad Sci U S A. 1995; 92:9697–9701. [PubMed: 7568200]

Mukamel EA, Nimmerjahn A, Schnitzer MJ. Automated analysis of cellular signals from large-scale calcium imaging data. Neuron. 2009; 63:747–760. [PubMed: 19778505]

Namburi P, Beyeler A, Yorozu S, Calhoon GG, Halbert SA, Wichmann R, Holden SS, Mertens KL, Anahtar M, Felix-Ortiz AC, et al. A circuit mechanism for differentiating positive and negative associations. Nature. 2015; 520:675–678. [PubMed: 25925480]

Okuyama T, Kitamura T, Roy DS, Itohara S, Tonegawa S. Ventral CA1 neurons store social memory. Science. 2016; 353:1536–1541. [PubMed: 27708103]

Padilla-Coreano N, Bolkan SS, Pierce GM, Blackman DR, Hardin WD, Garcia-Garcia AL, Spellman TJ, Gordon JA. Direct Ventral Hippocampal-Prefrontal Input Is Required for Anxiety-Related Neural Activity and Behavior. Neuron. 2016; 89:857–866. [PubMed: 26853301]

Parfitt GM, Nguyen R, Bang JY, Aqrabawi A, Tran MM, Seo DK, Richards BA, Kim JC. Bidirectional Control of Anxiety-Related Behaviours in Mice: Role of Inputs Arising from the Ventral Hippocampus to the Lateral Septum and Medial Prefrontal Cortex. Neuropsychopharmacology. 2017

Paton JJ, Belova MA, Morrison SE, Salzman CD. The primate amygdala represents the positive and negative value of visual stimuli during learning. Nature. 2006; 439:865–870. [PubMed: 16482160]

Phillips RG, LeDoux JE. Differential contribution of amygdala and hippocampus to cued and contextual fear conditioning. Behav Neurosci. 1992; 106:274–285. [PubMed: 1590953]

Pnevmatikakis EA, Soudry D, Gao Y, Machado TA, Merel J, Pfau D, Reardon T, Mu Y, Lacefield C, Yang W, et al. Simultaneous Denoising, Deconvolution, and Demixing of Calcium Imaging Data. Neuron. 2016; 89:285–299. [PubMed: 26774160]

Radley JJ, Arias CM, Sawchenko PE. Regional differentiation of the medial prefrontal cortex in regulating adaptive responses to acute emotional stress. J Neurosci. 2006; 26:12967–12976. [PubMed: 17167086]

Resendez SL, Jennings JH, Ung RL, Namboodiri VM, Zhou ZC, Otis JM, Nomura H, McHenry JA, Kosyk O, Stuber GD. Visualization of cortical, subcortical and deep brain neural circuit dynamics during naturalistic mammalian behavior with head-mounted microscopes and chronically implanted lenses. Nat Protoc. 2016; 11:566–597. [PubMed: 26914316]

Royer S, Sirota A, Patel J, Buzsaki G. Distinct representations and theta dynamics in dorsal and ventral hippocampus. J Neurosci. 2010; 30:1777–1787. [PubMed: 20130187]

Samuels BA, Anacker C, Hu A, Levinstein MR, Pickenhagen A, Tsetsenis T, Madronal N, Donaldson ZR, Drew LJ, Dranovsky A, et al. 5-HT1A receptors on mature dentate gyrus granule cells are critical for the antidepressant response. Nat Neurosci. 2015; 18:1606–1616. [PubMed: 26389840]

Sesack SR, Deutch AY, Roth RH, Bunney BS. Topographical organization of the efferent projections of the medial prefrontal cortex in the rat: an anterograde tract-tracing study with Phaseolus vulgaris leucoagglutinin. J Comp Neurol. 1989; 290:213–242. [PubMed: 2592611]

Silva BA, Mattucci C, Krzywkowski P, Murana E, Illarionova A, Grinevich V, Canteras NS, Ragozzino D, Gross CT. Independent hypothalamic circuits for social and predator fear. Nat Neurosci. 2013; 16:1731–1733. [PubMed: 24212674]

Skaggs WE, McNaughton BL, Wilson MA, Barnes CA. Theta phase precession in hippocampal neuronal populations and the compression of temporal sequences. Hippocampus. 1996; 6:149–172. [PubMed: 8797016]

Sotres-Bayon F, Quirk GJ. Prefrontal control of fear: more than just extinction. Curr Opin Neurobiol. 2010; 20:231–235. [PubMed: 20303254]

Strange BA, Witter MP, Lein ES, Moser EI. Functional organization of the hippocampal longitudinal axis. Nat Rev Neurosci. 2014; 15:655–669. [PubMed: 25234264]

Tannenholz L, Jimenez JC, Kheirbek MA. Local and regional heterogeneity underlying hippocampal modulation of cognition and mood. Front Behav Neurosci. 2014; 8:147. [PubMed: 24834033]

Tye KM, Prakash R, Kim SY, Fenno LE, Grosenick L, Zarabi H, Thompson KR, Gradinaru V, Ramakrishnan C, Deisseroth K. Amygdala circuitry mediating reversible and bidirectional control of anxiety. Nature. 2011; 471:358–362. [PubMed: 21389985]

Ulrich-Lai YM, Herman JP. Neural regulation of endocrine and autonomic stress responses. Nat Rev Neurosci. 2009; 10:397–409. [PubMed: 19469025]

Uwano T, Nishijo H, Ono T, Tamura R. Neuronal responsiveness to various sensory stimuli, and associative learning in the rat amygdala. Neuroscience. 1995; 68:339–361. [PubMed: 7477945]

Vong L, Ye C, Yang Z, Choi B, Chua S Jr, Lowell BB. Leptin action on GABAergic neurons prevents obesity and reduces inhibitory tone to POMC neurons. Neuron. 2011; 71:142–154. [PubMed: 21745644]

Wang DV, Wang F, Liu J, Zhang L, Wang Z, Lin L. Neurons in the amygdala with response-selectivity for anxiety in two ethologically based tests. PLoS One. 2011; 6:e18739. [PubMed: 21494567]

Wu MV, Hen R. Functional dissociation of adult-born neurons along the dorsoventral axis of the dentate gyrus. Hippocampus. 2014; 24:751–761. [PubMed: 24550158]

Xu C, Krabbe S, Grundemann J, Botta P, Fadok JP, Osakada F, Saur D, Grewe BF, Schnitzer MJ, Callaway EM, et al. Distinct Hippocampal Pathways Mediate Dissociable Roles of Context in Memory Retrieval. Cell. 2016; 167:961–972 e916. [PubMed: 27773481]

Zhou P, Resendez SL, Rodriguez-Romaguera J, Jimenez JC, Neufeld SQ, Stuber GD, Hen R, Kheirbek MA, Sabatini BL, Kass RE, Paninski L. Efficient and accurate extraction of in vivo calcium signals from microendoscopic video data. 2016 arXiv Prepr, arXiv1605.07266.

Ziv Y, Burns LD, Cocker ED, Hamel EO, Ghosh KK, Kitch LJ, El Gamal A, Schnitzer MJ. Long-term dynamics of CA1 hippocampal place codes. Nat Neurosci. 2013; 16:264–266. [PubMed: 23396101]

Highlights

Anxiogenic stimuli are differentially represented along the DV axis of the HPC

Inhibition of the vHPC in anxiogenic environments reduces avoidance behavior

vCA1 outputs to LHA but not BA control anxiety-related behavior

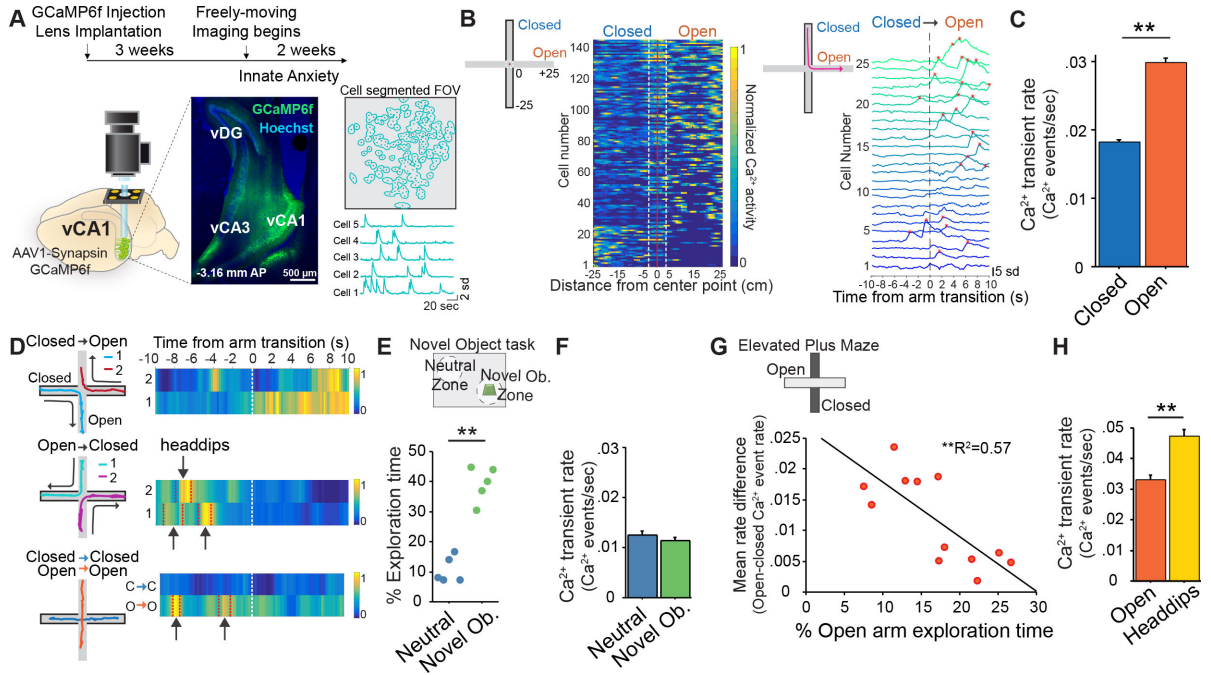The majority of vCA1-LHA projection neurons represent anxiogenic stimuli.

Figure 1. Representations of anxiety-related information in vCA1

(A) Experimental design for vCA1 freely-moving Ca^{2+} imaging. GCaMP6f was virally expressed and a GRIN lens implanted to target the CA1 pyramidal layer (middle image). Right, representative cell contours from a segmented Ca^{2+} video FOV. Right bottom, extracted Ca^{2+} transients from 5 example vCA1 neurons.

(B) Left, normalized Ca^{2+} activity from individual vCA1 neurons in the Elevated Plus Maze (EPM) in an example FOV, binned by distance (cm) from the EPM center point (red dot on EPM diagram) into either the open or closed arms. The majority of cells are more active in the open arm compartment (cells are sorted by location of peak Ca^{2+} activity bin (Closed arm: cells 1-26, Open arm/center: cells 27: 146), and activity spread throughout the maze (# of bins with 20% of peak Ca^{2+} activity)). Right, vCA1 Ca^{2+} transients from an example FOV during a behavioral transition between the closed and open arm compartment (transition at time 0 sec). Red asterisks indicate timing and peak of identified Ca^{2+} transient events.

(C) Rate of vCA1 neuron Ca^{2+} transients was significantly higher in the EPM open arms compared to closed arms (Wilcoxon sign rank, Z=−17.013, p<0.0001, N_{cells}=2,137).

(D) Left, example behavioral trajectories between arm compartments. Right, heatmaps of vCA1 normalized Ca^{2+} activity during those trajectories (each heatmap-trajectory pair is from the same FOV). Red dotted lines indicate a head-dip behavioral event in the open arm (also marked with arrows).

(E) Top, Novel object task design. Bottom, mice spend significantly more time exploring the novel object than the neutral zone (paired t-test, t_4=−8.594, p<0.01, N_{mice}=5).

(F) vCA1 Ca^{2+} transient rates are not significantly different between novel object and neutral zone (Wilcoxon sign rank, Z=−0.125, p=0.90, N_{cells}=677).

(G) Mean Ca^{2+} transient rate difference (open-closed) across an FOV is correlated with the anxiety state of the subject (% time in open arm) (linear regression, $F(1,10)=13.467$, $p<0.01$, $R^2=0.57$, $N_{mice}=12$).

(H) Rate of Ca^{2+} transients is higher during headdip behaviors relative to open arm (Wilcoxon sign rank, $Z=-7.251$, $p<0.0001$, $N_{cells}=400$).
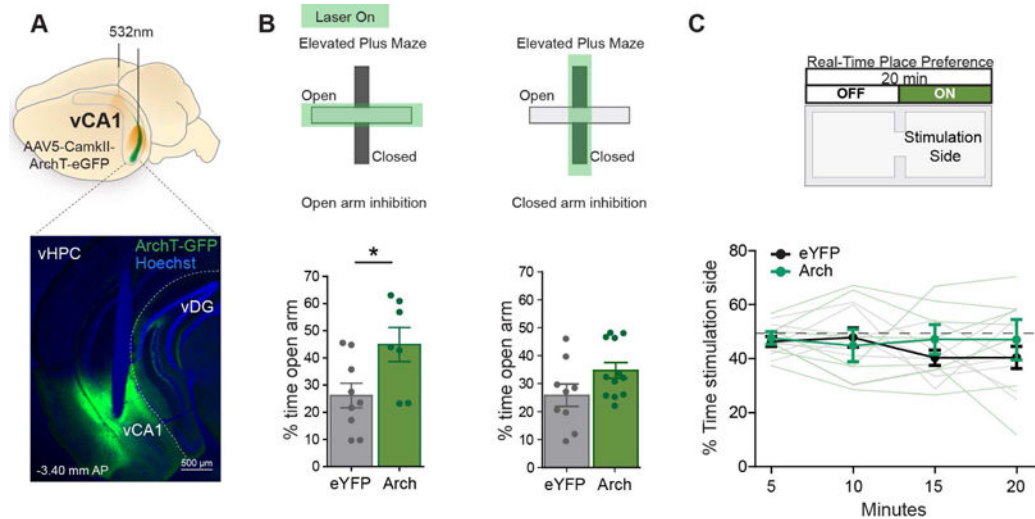
All data error bars represent mean $+/-$ SEM

Figure 2. Real-time control of avoidance behavior by vCA1

(A) Bilateral optogenetic silencing of CamKII-Arch expressing vCA1 neurons. Bottom, Representative placement of fiber optic.

(B) Left, In the EPM, the laser was triggered-on when mice entered the open arm only, and open arm silencing significantly increased % time exploration of the open arm, while silencing in the EPM closed arm (right panel) had no effect (EPM ANOVA $F_{(1,14)}$=6.184, p<0.05, N_{eYFP}=9, N_{Arch}=7; EPM ANOVA $F_{(1,19)}$=3.465, p=0.08, N_{eYFP}=9, N_{Arch}=12).

(C) RTPP, laser was triggered-on when mice entered one side of the identical 2-chamber arena, and mice showed no preference for % time exploration of the stimulation side. (ANOVA $F_{(1,13)}$=0.435, p=0.52, N_{eYFP}=8, N_{Arch}=7)
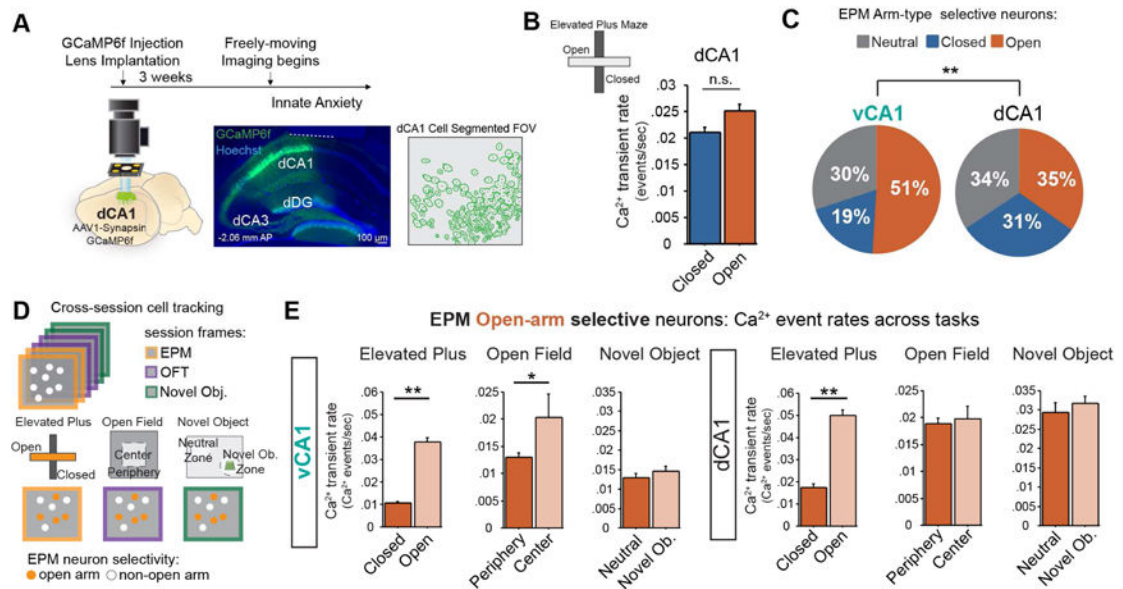
All data error bars represent mean +/− SEM

Figure 3. Differential representations of anxiety-related information along the dorsoventral axis of CA1

(A) Experimental design for dCA1 Ca^{2+} imaging. Left image, dCA1 GCaMP6f and GRIN representative lens placement. Right image, Representative contours of identified cellular units from a dCA1 imaging FOV.

(B) dCA1 rate of Ca^{2+} transients in the EPM. dCA1 neurons did not significantly increase their rate of Ca^{2+} transients to the open arm compartment (Wilcoxon signed rank Z=−1.451 p=0.15, N$_{dCA1}$=408).

(C) vCA1 is enriched in cells that are significantly selective for the EPM open arm compared to shuffle (orange pie chart; see methods), relative to dCA1 (Chi squared test of proportions $\chi^2(2)$= 43.984, p<0.0001 N$_{dCA1}$=408, N$_{vCA1}$=2,137).

(D) Analysis design. Top, imaging sessions from individual mice (imaged at a constant FOV) were concatenated into one large video prior to motion correction and cell segmentation to allow for cross-session cell tracking in different tasks (video frame edge-color denotes different imaging sessions combined; EPM: orange, OFT: purple, Novel Object task: green). Bottom, EPM open arm selective cells were then defined as in Fig. 3C, and their Ca^{2+} transient rates were compared across other imaging sessions.

(E) The Ca^{2+} transient rates of EPM open arm selective cells in vCA1 (left panels) and dCA1 (right panels) were compared in the EPM, OFT, and Novel Object tasks. vCA1 open arm selective cells were significantly more active to the EPM open arm and OFT center zones compared to the safe closed arm and periphery compartments (left two bar graphs), but did not change activity to exploration of a Novel Object (right bar graph) (vCA1 open arm cells: EPM open versus closed Wilcoxon signed rank Z=−12.016, p<0.0001; OFT center versus periphery rates Wilcoxon signed rank Z=−2.103, p<0.05; Novel Object Wilcoxon signed rank Z=−1.069, p=0.28; N$_{cells}$=192). In contrast, dCA1 open arm selective cells did not exhibit any changes in Ca^{2+} transient rate in the OFT center and Novel Object task, indicating that while vCA1 open arm neurons exhibit heightened activity across multiple tasks of innate anxiety, dCA1 open arm selective neurons are context-specific (dCA1 open arm cells Wilcoxon signed rank: EPM open versus closed Z=−10.338,

p<0.0001; OFT center versus periphery Z=−1.651, p=0.10; Novel Object rates Z=−1.242, p=0.21; N_{cells}=142).
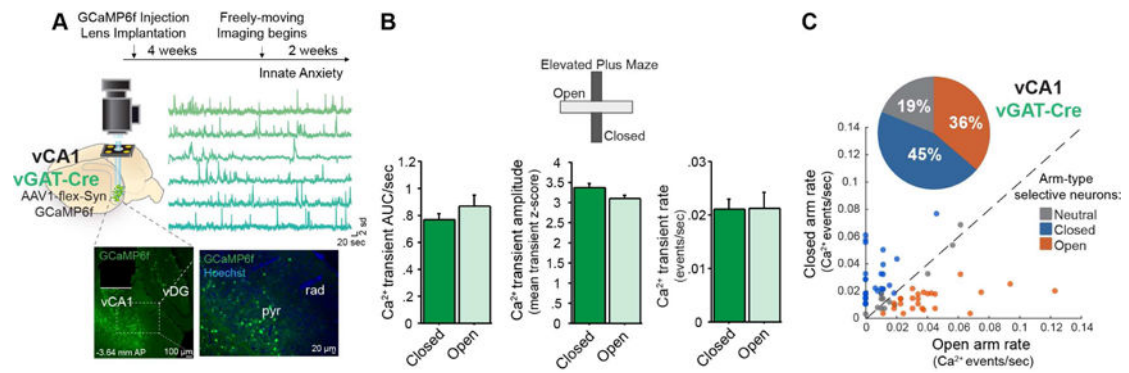
All data error bars represent mean +/− SEM

Figure 4. vCA1 inhibitory interneurons are not recruited during open arm exploration

(A) Experimental design for vCA1-vGAT Ca^{2+} imaging. Bottom left image, vCA1-vGAT-Cre/flex-GCaMP6f expression and representative GRIN lens placement; Bottom right image is a magnified inset of left. Top panel, extracted Ca^{2+} transients from an example vCA1-vGAT FOV.

(B) vCA1-vGAT Ca^{2+} activity in the EPM is not different between arm-types (N_{cells}=70 for all analyses). Left: Ca^{2+} transient area under the curve (AUC)/second (Wilcoxon sign rank Z=−0.781, p=0.43). Middle: mean Ca^{2+} transient amplitude (Wilcoxon sign rank Z=−1.505, p=0.13). Right: rate of Ca^{2+} transients (Wilcoxon sign rank Z=−0.451, p=0.65).

(C) vCA1-vGAT neurons are enriched in closed-arm selective cells (exceeding shuffle distribution rates) in the EPM. Scatter plot showing individual vCA1-vGAT neuron open vs closed rates, colored based on arm-type selectivity determined by exceeding shuffle distribution. Left pie chart inset is a summary of the scatter plot data.
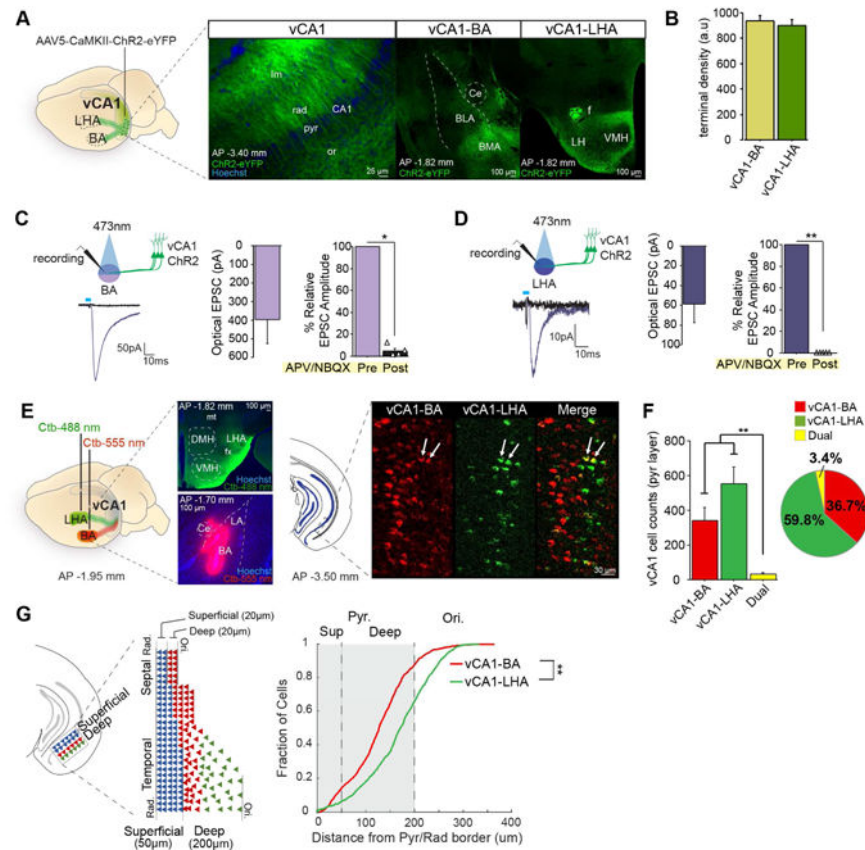
Figure 5. Separate populations of vCA1 neurons project to the Basal Amygdala and Lateral Hypothalamus

(A) Anterograde tracing of vCA1 axon terminals. CamKII-ChR2-eYFP virus was injected into vCA1 (left), and ChR2-eYFP axon terminals were visualized in the BA (middle) and LHA subfields (right).

(B) Average fluorescence of ChR2-eYFP terminal fields were similar between BA and LHA fields (paired t-test, $t_{(4)}=1.886$, p=0.13, $N_{mice}=5$)

(C) In vitro slice recordings of BA cells in ChR2-eYFP vCA1 injected mice. 5ms 473nm light pulses elicited large optical EPSC (mean onset latency= 0.93 ms +/− 0.12 SEM; purple example trace, middle bar graph, $N_{cells}=10$), which were abolished by APV/NBQX infusion (black example trace; right bar graph Mann Whitney U=0.00, p<0.05, $N_{cells}=4$)

(D) In vitro slice recordings of LHA cells in ChR2-eYFP vCA1 injected mice. 5ms 473nm light pulses elicited large optical EPSC (mean onset latency= 1.56 ms +/− 0.09 SEM; purple example trace, middle bar graph, $N_{cells}=10$), which were abolished by APV/NBQX infusion (black example trace; right bar graph Mann Whitney U=0.00, p<0.01, $N_{cells}=5$)

(E) Ctb retrograde labeling of vCA1 projections to the BA (Ctb-555) and LHA (Ctb-488). Left, representative images of CTB injection sites in the BA (bottom) and LHA (top). Right, representative image of retrogradely labeled vCA1 neurons projecting to BA (red cells), LHA (green cells) or both (yellow cells, white arrows).

(F) Quantification of retrogradely labeled vCA1 neurons. vCA1-BA and LHA projecting neurons are largely non-overlapping as only ~3% of counted cells were dual-labeled (paired

t-tests BA or LHA vs Dual, BA vs Dual t(10)=4.309, LHA vs Dual t(10)=5.832, p<0.01 for both).

(G) Left diagram, CA1 deep and superficial lamination. Right, cumulative distribution of vCA1-BA (red line) or vCA1-LHA (green line) labeled neuron distances from the inner radial border. The vCA1-LHA neuron distance distribution was significantly right shifted relative to vCA1-BA neurons, indicating that LHA neurons are organized deeper in the CA1 pyramidal layer (KS test, p<0.0001, KS stat=0.2999).

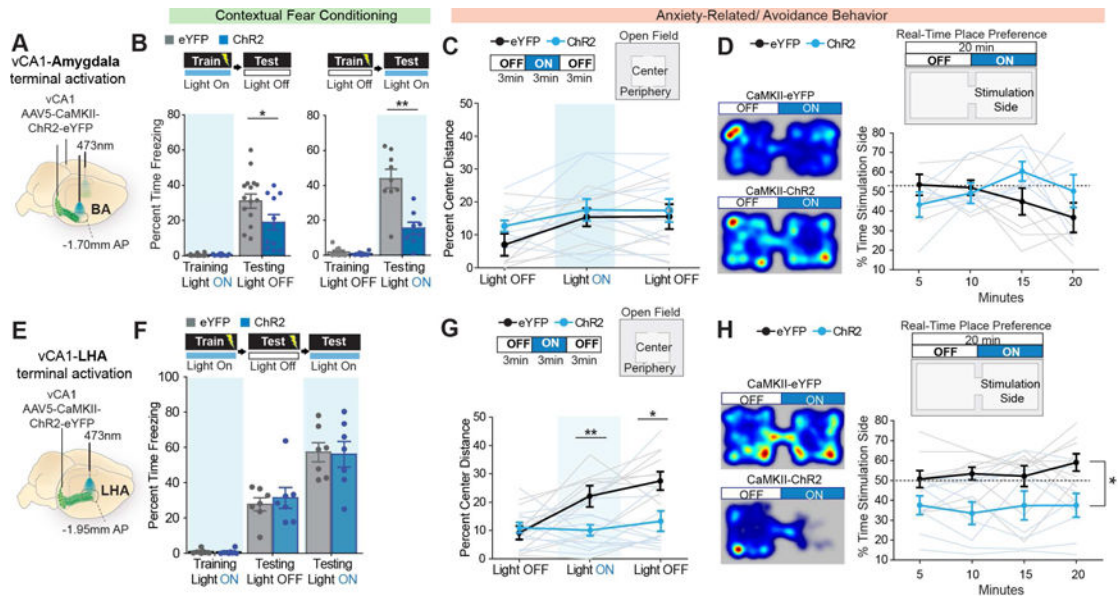All data error bars represent mean +/− SEM

Figure 6. vCA1-Amygdala and vCA1-LHA projectors differentially contribute to anxiety-related behavior and learned fear

(A) Experimental design of bilateral vCA1-amygdala terminal ChR2 optogenetic stimulation (targeting the basal amygdala).

(B) vCA1-amygdala ChR2-eYFP optogenetic terminal stimulation (473nm 10hz, 5ms pulses) during CFC encoding (left panel, training light on) and CFC retrieval (right panel, testing light on). Stimulation of vCA1-BA terminals on training day 1 or testing day 2 reduces % time freezing, indicating a disruption of both CFC encoding and retrieval (repeated measures anova, % time freezing*genotype interaction; training light on (left panel) $F_{(1,24)}$=6.358, p<0.05, N_{eYFP}=15, N_{ChR2}=11; testing light on (right panel) $F_{(1,15)}$=21.10, p-value<0.001, N_{eYFP}=9, N_{ChR2}=8).

(C) vCA1-BA ChR2-eYFP optogenetic terminal stimulation in OFT in 3 min laser epochs (light off-on-off; light on: 473nm 20hz, 5ms pulses) had no impact on % center distance (Repeated measures ANOVA, $F_{(1,16)}$=0.497, p=0.61, N_{eYFP}=7, N_{ChR2}=11).

(D) vCA1-amygdala ChR2-eYFP optogenetic terminal stimulation in RTPP (473nm 20hz, 5ms pulses, laser triggered on in one chamber only). Left panel, RTPP chamber occupancy heatmaps of representative eYFP and ChR2 mice. Right graph, ChR2 stimulation did not impact % time on stimulation side, indicating that the stimulation was neither appetitive nor aversive (5 min bins, ANOVA % time stim*genotype, $F_{(1,11)}$=0.573, p=0.46, N_{eYFP}=8, N_{ChR2}=5).

(E) Experimental design of bilateral vCA1-LHA terminal ChR2 optogenetic stimulation.

(F) vCA1-LHA ChR2-eYFP optogenetic terminal stimulation (473nm 10hz, 5ms pulses) during CFC encoding (left bar graph, training light on) and CFC retrieval (right bar graph, testing light on), had no impact on % time freezing on either testing day (Repeated measures ANOVA, $F_{(1,12)}$=0.216, p=0.81, N_{eYFP}=7, N_{ChR2}=7).

(G) vCA1-LHA ChR2-eYFP optogenetic terminal stimulation in OFT in 3 min laser epochs (light off-on-off; light on: 473nm 20hz, 5ms pulses) significantly reduced % center distance relative to controls (ChR2: blue line, Repeated measures ANOVA; % center

distance*genotype interaction, $F_{(1,19)}=7.635$, $p<0.01$; light on ANOVA $F_{(1,19)}=9.356$, $p<0.01$; light off epoch 3 ANOVA $F_{(1,19)}=7.981$, $p<0.05$; $N_{eYFP}=9$, $N_{ChR2}=12$).

(H) vCA1-LHA ChR2-eYFP optogenetic terminal stimulation in RTPP (473nm 20hz, 5ms pulses, laser triggered on in one chamber only). Left panel, RTPP chamber occupancy heatmaps of representative eYFP and ChR2 mice. Right graph, ChR2 stimulation significantly decreased % time on stimulation side, indicating that the stimulation was aversive (5 min bins, ANOVA, % time stim*genotype $F_{(1,15)}=8.403$, $p<0.05$; $N_{eYFP}=9$, $N_{ChR2}=8$).
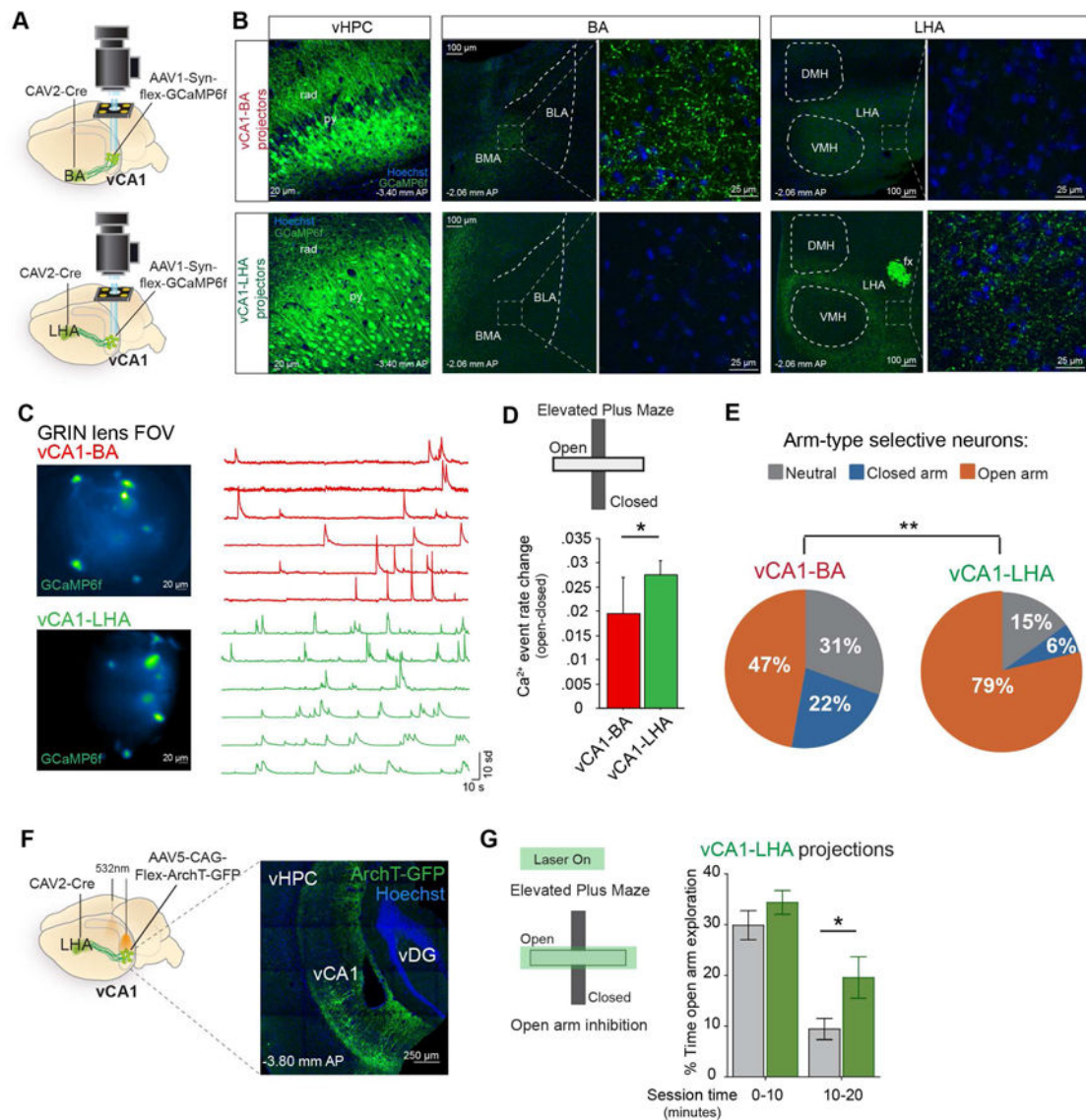
All data error bars represent mean +/− SEM

Figure 7. The vCA1-LHA projection is enriched in anxiety cells

(A) Projection-specific Ca^{2+} imaging experimental design, CAV2-Cre was injected into either BA (top) or LHA (bottom), and flex-GCaMP6f was injected into vCA1 to express GCaMP6f in vCA1-BA or vCA1-LHA projection neurons specifically.

(B) Dual viral targeting of projection specific vCA1 neurons allowed for selective expression of GCaMP6f in vCA1-BA (top panel) or vCA1-LHA (bottom panel) neurons only. This was confirmed by visualization of fluorescent terminals in the BA but not LHA subfield of vCA1-BA labeled mice (top middle and right panels), and fluorescent terminals in the LHA but not BA subfields in vCA1-LHA labeled mice (bottom middle and right panels).

(C) Representative GRIN lens FOV from vCA1-BA (top) and vCA1-LHA GCaMP6f (bottom) labeled mice. Right, example of extracted Ca^{2+} transients from projection specific vCA1-BA (top, red traces), and vCA1-LHA (bottom, green traces) labeled FOV.

(D) Ca^{2+} transient rate difference (open-closed) in EPM between projection-specific populations. vCA1-LHA projection neurons exhibited significantly greater rate changes in the EPM open arm compartments (Mann Whitney U=1097.00, p<0.05. N_{BA}=36, N_{LHA}=80).

(E) vCA1-LHA projection neurons are enriched in cells that are significantly selective for the EPM open arm compared to shuffle (orange pie chart; see Fig S6C and methods), relative to vCA1-BA projectors (Chi squared test of proportions, χ^2(2)=11.45, p<0.01 N_{BA}=36, N_{LHA}=80).

(F) Experimental design, CAV2-Cre was injected into the LHA, and Cre-dependent ArchT-GFP was injected into vCA1 to selectivity express Arch in vCA1-LHA projections bilaterally. Optogenetic fibers were implanted at the vCA1 injection site.

(G) vCA1-LHA projections were silenced during EPM open arm exploration bouts (laser turned on in open arm only), which significantly decreased open arm avoidance relative to eYFP controls (ANOVA mins 10-20; $F_{(1,17)}$=5.195, p<0.05, N_{eYFP}=10, N_{Arch}=9).

All data error bars represent mean +/− SEM